ASSESSING THE ABILITY OF COUPLED MODEL INTERCOMPARISON PROJECT PHASE 5 (CMIP5) MODELS TO CAPTURE CONNECTIONS BETWEEN GREAT BASIN PRECIPITATION AND PACIFIC OCEAN MODES OF VARIABILITY AND APPLYING THE ASSESSMENT INTO THE FUTURE

by

Kimberly L. Smith

A thesis submitted to the faculty of
The University of Utah
in partial fulfillment of the requirements for the degree of

Master of Science

Department of Atmospheric Sciences

The University of Utah

May 2015

The University of Utah Graduate School

STATEMENT OF THESIS APPROVAL

The thesis of **Kimberly L. Smith**

has been approved by the following supervisory committee members:

Courtenay Strong	, Chair	**10/10/14** Date Approved
Thomas Reichler	, Member	**10/10/14** Date Approved
Simon Wang	, Member	**10/10/14** Date Approved

and by **Kevin Perry** , Chair/Dean of

the Department/College/School of **Atmospheric Sciences**

and by David B. Kieda, Dean of The Graduate School.

ABSTRACT

Precipitation over the Wasatch Mountain Range of northern Utah, part of the Great Basin (GB) in the western United States, provides water for millions of people living along the Wasatch Front. Western US precipitation is known to be influenced by the El-Niño–Southern Oscillation (ENSO) as well as the Pacific Decadal Oscillation (PDO) in the North Pacific. Historical connectivity between GB precipitation and Pacific Ocean sea surface temperatures (SSTs) on interannual to multidecadal time scales is evaluated for 20 models that participated in the Coupled Model Intercomparison Project Phase 5 (CMIP5). While the majority of the models had realistic ENSO and PDO spatial patterns in the SSTs, the simulated influence of these two modes on GB precipitation tended to be too strong for ENSO and too weak for PDO. Few models captured the connectivity at a quasi-decadal period influenced by the transition phase of the Pacific quasi-decadal oscillation (QDO; a recently identified climate mode that regulates GB precipitation). Some of the discrepancies appear to stem from models not capturing the observed tendency for the PDO to modulate the sign of the ENSO–GB precipitation teleconnection. Of all of the models, CCSM4 most consistently captured observed connections between Pacific SST variability and GB precipitation on all time scales, suggesting that in

future applications, its output represents a higher confidence for the future climate of this region. The utility of the assessment is illustrated by a brief statistical analysis of future western US precipitation under a high emissions scenario.

Using the results from the assessment, the application portion of the study analyzes future precipitation data under a high emissions scenario (RCP 8.5) to determine what the future could potentially look like over the western US. The models are ranked based on their performance in capturing the connections between GB precipitation and Pacific Ocean modes of variability. The ranking then determines which model would be appropriate to be applied to a stochastic framework and dynamical downscaling analyses. The results from the assessment were used to force a nonstationary, daily stochastic weather generator and produce precipitation occurrence output for a valley site and a mountain site located within the GB. With some considerations, the stochastic weather generator provides long-term data for any time period that statistically matches the input data.

TABLE OF CONTENTS

LIST OF FIGURES

ACKNOWLEDGEMENTS

This material is based upon work supported by the National Science Foundation under grants EPS-1135482, EPS-1135483, and EPS-1208732. Any opinions, findings, and conclusions or recommendations expressed in this material are those of the authors and do not necessarily reflect the views of the National Science Foundation. Additional support for K. Smith was provided by the University of Utah, including a fellowship from the Global Change and Sustainability Center. Provision of computer infrastructure by the Center for High Performance Computing at the University of Utah is gratefully acknowledged.

CHAPTER 1

INTRODUCTION

The Introduction is composed of two sections, the first being a literature review about precipitation drivers that affect the Great Basin and the connectivity patterns used to evaluate the Coupled Model Intercomparison Project Phase 5 (CMIP5) models. The second section reviews literature about stochastic weather simulators, which are one of the applications of the model assessments.

1.1 Assessment of CMIP5 Models

Precipitation variability in present and future climate scenarios has important impacts on local and regional hydrology, ultimately influencing water availability. Year-to-year fluctuations in precipitation, especially winter snowfall in mountainous terrain, create challenges for water managers. The Great Basin (GB) watershed is located in the interior western United States (comprises parts of Utah, Wyoming, Idaho, Oregon, Nevada, and California) and is made up of many smaller snowpack-dominated watersheds, including that of the Great Salt Lake (GSL) in northern Utah. The GSL basin, which encompasses the Wasatch Mountain Range, is subjected to

substantial interannual and multidecadal precipitation variability (Ropelewski and Halpert, 1986; Wang et al., 2010, 2012). Droughts are common in the semi-arid GSL basin (Cook et al., 2004). Orographic precipitation that occurs in the Wasatch Range is stored as snowpack and then delivered as runoff to the Wasatch Front, where over two million people live and work.

The knowledge of precipitation drivers in the GSL basin (and the GB) is an important tool for local water managers to guide water managing and infrastructure engineering in preparation for drought or flooding. The GSL basin is situated in the transition boundary of the winter weather pattern that is forced by the El Niño-Southern Oscillation (ENSO), known as the ENSO dipole or North American dipole, suggesting that ENSO has both positive and negative effects on the precipitation received in the basin (Wang et al., 2010; Wise, 2010). For much of the 20th century, El Niño is generally associated with a wet, cool southwestern US and a dry, warm northwestern US, while La Niña is associated with the opposite (Ropelewski and Halpert, 1986; Dettinger et al., 1998). It is well known that the Pacific decadal oscillation (PDO), defined as the leading principal component of monthly north central Pacific SST variability (poleward of 20°N; Mantua et al., 1997), has a significant effect on western US precipitation. The PDO is linked to, and can modulate, the phasing of ENSO and together can result in prominent precipitation anomalies in the western US (Gershunov and Barnett, 1998; Gershunov et al., 1999; Mauget, 2003). The PDO-ENSO coupling results in a shift of the precipitation dipole over the western US (Wise, 2010; Brown, 2011). Because the GB is situated in the

transition of the ENSO dipole, which shifts its wet/dry influences based on the phase of the PDO, it is important to determine how the warming climate will affect the PDO-ENSO teleconnection and the precipitation received in the basin.

The elevation of the GSL has recorded the primary climate cycles in the GB. Examining GSL elevations, previous studies have revealed a predominant quasi-decadal oscillation (QDO) associated with precipitation and surface runoff (Wang et al., 2010). The GSL elevation is significantly coherent with the Pacific QDO, defined by anomalous sea surface temperatures (SSTs) in the Nino-4 region (5°S to 5°N, 160°E to 150°W). However, because it takes time for the GSL to integrate the precipitation change in the broad watershed, this aforesaid coherence between the Niño-4 and the GSL level means that precipitation in the GSL basin must be phase-shifted from the Pacific QDO by a quarter phase; this creates a lag of about three years between the Niño-4 and the precipitation (and between the precipitation and the GSL level) (Wang et al., 2010). During this transition phase of the Pacific QDO, a tropospheric short-wave train pattern forms in the Western Tropical Pacific and emanates towards North America (Wang et al., 2011). This standing short-wave train is associated with enhanced precipitation in the Intermountain West, hence explaining the quarter-phase lagged response of precipitation to the Pacific QDO.

There has been an increased interest in the effects that climate change may have on GB hydrology (e.g. Bardsley et al., 2013; Mensing et al., 2013). Climate change assessments rely heavily on climate models. The latest generation of global climate models (GCMs) participating in the Coupled Model Intercomparison Project Phase 5

(CMIP5) contributed importantly to the recently published Intergovernmental Panel on Climate Change (IPCC) Assessment Report 5 (AR5; IPCC, 2013). In addition to the atmosphere-ocean global climate models (AOGCMs), this generation of GCMs includes what are known as Earth system models (ESMs), which are AOGCMs coupled with the carbon cycle fluxes between the ocean, atmosphere, and land surface (Taylor et al., 2011). Other advancements with CMIP5 include more models, an increased number of experiments and outputs, and enhanced physics packages (Taylor et al., 2011).

Chapter 2 assesses 20 models that participated in CMIP5. Each of the 20 models was evaluated based on the connections between interdecadal to multidecadal historical Pacific Ocean SST variability and precipitation in the Great Basin. This chapter outlines the methods used to complete the assessment, and the results presented were then applied to an analysis of climate data into the future. This chapter has been conditionally accepted in the Journal of Climate.

1.2 Applying Results of Model Assessment

As mentioned in the previous section, the semi-arid climate of the Great Basin is highly affected by year-to-year variations in precipitation. Because millions of people are affected by the snowpack stored in the high terrain of the Wasatch Mountain Range and western Uinta Mountains, which feeds directly into the valleys from Logan to Provo, UT, it is imperative to understand the long-term effects of potential changes in the hydrology due to the precipitation variations. As we look into the future,

these precipitation variations could be largely affected by warming temperatures. Increased temperatures may not change the amount of precipitation received in the high terrain, but it is likely that more precipitation will fall as rain than as snow in the winter months, resulting in reduced snowpacks (Barnett et al., 2005). Additionally, the spring runoff may come earlier than usual, putting stress on the reservoir systems (Barnett et al., 2005). With these possibilities in mind, it is of interest to simulate future weather data with a stochastic framework based on realistic simulations of past and present weather data.

The first studies using stochastic simulators of weather data employ two-state, first-order Markov chain frameworks regarding precipitation (Bailey, 1964; Richardson, 1981; Roldàn and Woolhiser, 1982), meaning that the probability of precipitation occurrence on a given day is only dependent on whether precipitation occurred or not on the previous day. Precipitation amount was modeled separately, and maximum/minimum temperatures and solar radiation were modeled as a function of precipitation occurrence. Other studies involving stochastic weather generators considered a two-state, second-order Markov chain process (Stern and Coe, 1984; Wilks, 1999a). Markov chains of higher order have been found to better capture dry spells than first-order Markov chains, thus providing more accurate results for most areas of the western US where dry spells are common, such as the semi-arid Great Basin.

One limitation of the common stochastic weather generators is the ability to successfully capture nonstationary variability. In general, the use of the Markov chain

analysis assumes stationarity. Previous studies have found that over the western US, El Niño results in a wetter Southwest and a drier Northwest, while La Niña results in the opposite (Ropelewski and Halpert, 1986; Dettinger et al., 1998; Woolhiser, 2008). In addition, the PDO also has significant impacts on precipitation in the western US. As discussed previously, the PDO is linked to ENSO, which in turn affects how the different phases of ENSO will impact the western US. Woolhiser (2008) introduces the idea of adding nonstationarity to the stochastic framework in order to rectify the effects these major oceanic oscillations have on western US precipitation. Essentially, perturbations given as time series of the oscillations (plus a trend) were linearly added to the probability of precipitation, and the coefficients associated with each perturbation give information on the sensitivity of each of the oscillations (Woolhiser, 2008).

For analyses covering a relatively large domain and spanning major differences in terrain, creating multisite stochastic weather generators is necessary to more realistically model the weather, which can be highly spatially dependent. Brissette et al. (2007) completed a study based on the multisite stochastic weather generator constructed by Wilks (1998) and built on the work by presenting an algorithm which involves a "brute force" iterative process using a perturbation equation added to the observed correlation matrix of rainfall occurrence. The observed correlation matrix was used to generate synthetic data through the Markov chain process and result in a synthetic correlation matrix. The perturbation addition was necessary to increase the precision and result in a true minimization of the data over an arbitrary

number of sites. Wilks (2009) showed that spatially interpolating stochastic weather generators at individual locations is statistically feasible. By applying the standard Gaussian parameters determined from the multisite weather generator, Wilks (2009) was also able to synchronize the generator with real weather data and simulate realistic weather data over those sites for particular years.

Chapter 3 starts by applying the results from Chapter 2 to a brief statistical analysis of future precipitation data over the western US under a high emissions scenario (RCP 8.5). Then, 151 years of downscaled daily precipitation data from the CCSM4 model (including both historical and future data) is used to force the nonstationary, daily stochastic weather generator. The stochastic weather generator involves a two-state, second-order Markov chain for determining precipitation occurrence, introduces nonstationarity to assess its importance over the domain, and allows for more realistic simulation by applying the framework over multiple sites. For this study, the sole focus is on precipitation occurrence. Chapter 4 includes the discussion and conclusions for Chapter 2 and Chapter 3.

CHAPTER 2

ASSESSMENT OF CMIP5 MODELS

2.1 Introduction

In the western United States, the CMIP5 models tend to underestimate the precipitation variability on decadal to multidecadal time scales (Ault et al., 2012). Because the hydrology in the GB is driven both by the interannual variability (Dettinger et al., 1998) and by quasi-decadal variability (e.g. Wang et al., 2010, 2012), this study presents a CMIP5 model comparison focused on the interannual to multidecadal connections between historical Pacific Ocean SSTs and GB precipitation. Identification of CMIP5 models that realistically capture oceanic modulation of GB precipitation over a range of time scales is important for (a) informing an objective weighting of climate projections and (b) selecting models to be used in dynamical downscaling and/or stochastic climate modeling, thus providing climate information usable for collaborators in hydrology, biology, urban planning, and civil engineering. Moreover, because the projected precipitation changes disagree over the GB between CMIP5 and the previous generation of models (CMIP3), as was shown in (Brekke, 24 April 2013), there is an urgent need to evaluate the CMIP5 models

for the GB hydroclimate.

2.2 Data and Methods

2.2.1 Data

The observational precipitation data used in this study are 1° gridded monthly global land-surface precipitation data, which span from January 1901 to December 2010 (Schneider et al., 2011; http://gpcc.dwd.de/). The data are calculated from 67,200 global stations and provided by the Global Precipitation Climatology Centre (GPCC). The analysis domain chosen for this study follows (Wang et al., 2010) and encompasses the eastern Great Basin in the western United States (37.5-42.5°N and 115-110°W; Fig. 2.1). The eastern Great Basin contains the Wasatch Range, a major contributor of water flow in the Great Salt Lake basin. As noted in previous studies (e.g. Wang et al., 2010), even though the analysis domain covers more than just the eastern Great Basin, the low-frequency precipitation variability is consistent over the extent of this domain.

The observational sea surface temperature data used in this study (HadISST) are reconstructed 1° gridded monthly data based on in situ and satellite observations. The data span from January 1870 to June 2013 (Rayner et al., 2003) and were obtained from the UK Met Office Hadley Centre (MOHC).

For inclusion in the study, CMIP5 models were required to have the all-forcing historical precipitation output and sea surface temperature output, both back to at least 1900. The all-forcing experiments include both natural forcings and an-

thropogenic forcings. Twenty models satisfied this criterion, and Table 2.1 provides the modeling center, number of ensemble members, and literature references for each. The observational data analysis spans 1901-2005 to align with the GPCC precipitation data starting in 1901, and the model data spans 1900 to 2005. The year difference is negligible due to the filtering described immediately below.

2.2.2 Methods

In order to concentrate on the time scales of interest (i.e. the interannual and quasi-decadal frequencies), we filtered the precipitation and SST data three different ways using a Hamming Window (HW) filter (Hamming, 1998). As discussed in (Wang et al., 2010), this windowed filter is most appropriately applied to short-length time series because of its ability to essentially eliminate unwanted frequencies (Iacobucci and Noullez, 2005). We applied a 3-7-year bandpass filter to the data to determine the high frequency variability associated with ENSO. We applied a 10-15-year bandpass filter to obtain the quasi-decadal signal such as that which was found in (Wang et al., 2010). We applied a low-pass 7-year filter to analyze variability on multidecadal and longer timescales.

To define the Pacific Decadal Oscillation (PDO), we computed the leading empirical orthogonal function (EOF; Hannachi et al., 2007) of the detrended, low pass 7-year filtered monthly sea surface temperature data. The EOF analysis was performed over the northern Pacific Ocean (20-66°N, 160°E to 110°W) and yielded the well-known "horseshoe pattern" characterizing the PDO (e.g. Mantua et al.,

1997). We set the sign of the EOF to emulate the positive (warm phase) PDO pattern and regressed the sea surface temperatures onto the associated principal component time series, which gives units of Kelvin per standard deviation at each location (as opposed to the arbitrary scaling of the EOF; e.g. Thompson and Wallace, 2000).

In our results, we present maps of the correlation between filtered GB precipitation and SSTs on several timescales for each model. The map domain makes up most of the Pacific Ocean (40°S to 65°N; 90°E to 120°W). For all correlation analyses and displayed maps, the model data were bilinearly interpolated onto the same 1° grid corresponding to the SST observations. In order to determine the degree to which the model correlation maps matched the observations, we calculated the area-weighted uncentered spatial correlation (r_u):

$$r_u = \frac{\sum_{i=1}^{n} w_i c_i^o c_i^m}{\left[\sum_{i=1}^{n} w_i (c_i^o)^2 \sum_{i=1}^{n} w_i (c_i^m)^2\right]^{1/2}} \tag{2.1}$$

where w_i is an area weighting function, c_i^o is the observational data, and c_i^m is the model data interpolated on the same grid as the observational data for each location i (λ_i, ϕ_i) where λ is longitude and ϕ is latitude. This statistic was applied in Alexander and Arblaster (2009), and a similar statistic (referred to as congruence) was used in Kiktev et al. (2007). Where multiple ensemble members were available from a single model, the area-weighted uncentered spatial correlation was calculated for each ensemble member, and the member from each model that most closely matched the observational map is shown for discussion.

To analyze teleconnections, we computed the geostrophic streamfunction (ψ) over the North Pacific and North America:

$$\psi \propto \frac{Z_g}{f} \tag{2.2}$$

where Z_g is the 200 hPa geopotential height at a given location (λ_i, ϕ_i) and f is the Coriolis parameter $2\Omega \sin \phi_i$. We obtained NCEP/NCAR Reanalysis 1 monthly mean geopotential height data from 1948 to 2005 (Kalnay et al., 1996) to complete the observational streamfunction analysis. To show an example of variations in initial conditions in a model, we also calculated the streamfunction using monthly mean geopotential height data over the same time period for each CCSM4 ensemble member. The data were filtered with the HW bandpass 3-7-year and 10-15-year filter and then correlated with GB precipitation.

2.3 Results

2.3.1 Interannual (3-7-year) Pacific SSTs–GB precipitation relationship

Fig. 2.2 shows the interannual (3-7-year) contemporaneous correlation spatial patterns between SSTs and GB precipitation for each included CMIP5 model and observations. For observations (Fig. 2.2u), the contemporaneous correlation map of bandpass 3-7-year filtered Pacific SSTs and Great Basin precipitation highlights higher frequency Pacific Ocean variability dominated by ENSO in the tropics with variability also in the extratropics. In the CMIP5 ensemble, we show in Fig. 2.2 only the member from each model with the correlation map that best matches that of observations based on the area-weighted uncentered spatial correlation coefficients

(Eq. 2.1). As discussed in (Deser et al., 2014), internal variability within each model is very different. Most models, including CCSM4 and CESM1(CAM5.1, FV2), exhibit a stronger than observed correlation between the tropics and GB precipitation compared to observations (compare all panels to Fig. 2.2u). Despite being excessively strong in the tropics, the majority of the spatial patterns in the mapped ensemble members do resemble observations ($r_u \geq 0.5$, Fig. 2.3a; recall Eq. 2.1). However, a few of the models have additional ensemble members that do not capture the observed pattern as well (Fig. 2.3a; x symbols close to zero). In contrast, CCSM4 and CESM1(CAM5.1, FV2) are notable for consistency of r_u among members. The documented over-energetic nature of the GB precipitation–ENSO connection contributes to high variances in both GB precipitation and Niño-4 SST for several models with high r_u (e.g. MIROC5, CCSM4, CESM1(CAM5.1, FV2); Fig. 2.4a,d).

The relatively weak correlations in the observations between SSTs along the equatorial Pacific and GB precipitation (Fig. 2.2u) support the variable association between ENSO and GB precipitation due to the shifts of the dipole cancelling out the ENSO signal. Nearly all of the models capture the connection between the ENSO region and GB precipitation, but some of them (e.g. CCSM4 and CESM1(CAM5.1, FV2)) have a stronger correlation between warm ENSO SSTs and GB precipitation than what is observed.

The midlatitude storm track is known to be affected by sea surface temperatures in the North Pacific (e.g. Namias et al., 1988; Peng and Whitaker, 1999; Frankignoul et al., 2011), and we selected CCSM4 to analyze this more closely in part because

of its tightly packed set of r_u values across its ensemble members (Fig. 2.3a; x symbols). We calculated the 200-hPa streamfunction using geopotential height at 200 hPa, smoothed the data with the HW bandpass filter to focus on the 3-7-year and 10-15-year variability, and correlated it with GB precipitation to visualize associated dynamics in the North Pacific (Fig. 2.5). The bandpass 3-7-year filtered observational and averaged CCSM4 data have a negative correlation over the western US, indicating the overall trough anomalies observed in conjunction with precipitation in the Great Basin (Fig. 2.5a-b). The simulated low pressure in the upper North Pacific also seems consistent. However, the individual CCSM4 ensemble members exhibit notably variable streamfunction correlation patterns upstream of the western US (Fig. 2.5c-h). The variable streamfunction correlation patterns upstream from the GB in CCSM4 indicate that, even for a model with strong ENSO–GB precipitation correlation in general, the underlying storm track dynamics can vary internally.

2.3.2 Links between ENSO and the PDO

As noted in the introduction, there is evidence that the PDO modulates ENSO-driven precipitation over the western U.S. To analyze this effect in CMIP5, we computed the 10-year running correlation between the bandpass filtered 3-7-year spatially averaged Niño-4 SSTs and Great Basin precipitation for all models and the observations to depict decadal fluctuations in the ENSO teleconnection. The time series of the running ENSO–GB precipitation correlation (r_{EG}) was then compared to the PDO time series (the observational time series are shown in Fig. 2.6a), and a

correlation was calculated between the PDO and r_{EG} to determine the effect the PDO has on the connection between Niño-4 SSTs and GB precipitation. The results are shown in Fig. 2.6b. The observational data show a strong positive running correlation (r_{EG}) between Niño-4 SSTs and GB precipitation when the PDO is negative. The correlation between the PDO and r_{EG} is strongly negative because of this (observations bar; Fig. 2.6b), indicating that El Niño is conducive to precipitation in the Great Basin during negative (cool phase) PDO. When PDO is positive (warm phase), La Niña is conducive to precipitation in the Great Basin. In short, the PDO alters the sign of the ENSO–GB precipitation teleconnection.

To visualize the underlying dynamics, we calculated the correlation coefficients between the 200-hPa streamfunction and GB precipitation for the years of negative PDO (and consequently, high running correlation coefficients between Niño-4 SSTs and GB precipitation) (Fig. 2.5i). The trimodal pattern over the Pacific follows that described in Gill (1980) and Alexander et al. (2002) and reflects the canonical atmospheric response to El Niño. However, the composite map of all six CCSM4 ensemble members is nearly opposite to that of the observational map (Fig. 2.5j), and there is substantial variability among the individual members (Fig. 2.5k-p).

In general, the models are unable to capture the observed negative correlation between the PDO and r_{EG} (Fig. 2.6b). However, there are some models that have comparable negative correlations to observations. In CCSM4, the running correlation between Niño-4 SSTs and GB precipitation stays above zero for nearly the entire time period (not shown). In this case, negative PDO weakens the ENSO–precipitation

correlation but does not make it negative, resulting in the much higher overall correlation coefficient between Niño-4 SSTs and GB precipitation for CCSM4 (Fig. 2.3b). However, because the PDO in CCSM4 does modulate ENSO, the correlation coefficient between the PDO Index and r_{EG} is negative. The PDO in BCC-CSM1.1 modulates its ENSO as apparent by the correlation coefficient between the PDO Index and r_{EG} (Fig. 2.6b). BCC-CSM1.1 also has a correlation coefficient between Niño-4 SSTs and GB precipitation more comparable to that of observations (Fig. 2.3b). However, its spatial pattern does not match well with observations (Fig. 2.3a). By visual inspection, the map in Fig. 2.2b captures the majority of the observational pattern (Fig. 2.2u) and even the trimodal pattern in the North Pacific. This brings to light that because the area-weighted uncentered spatial correlation is one number that represents a large spatial pattern, there are limitations to using it. The models may display a pattern that is similar to observations but that is shifted spatially, which can reduce the r_u value significantly.

2.3.3 Quasi-decadal Pacific SSTs–GB precipitation relationship

The contemporaneous correlation maps between bandpass 10-15-year filtered SST data and GB precipitation data are generally similar in spatial extent and strength between the models (Fig. 2.7). Additionally, a large number of the models produce SST spatial patterns that are similar to the observations based on the relatively high area-weighted uncentered spatial correlations (Fig. 2.3b). While model agreement with observations seems good at a low frequency, the r_u values decrease more rapidly

across the models compared to the higher frequency mode and even become negative; this suggests a further challenge for models to capture the decadal-scale variability as observed. The various ensemble members of each model also performed variably, with an increased number of them having realizations opposite of that seen in observations (x symbols below zero in Fig. 2.3a-b); this suggests the nature of decadal-scale variability to be internal and stochastic (Guilyardi et al., 2009).

As with the high-frequency data, we calculated the 200-hPa streamfunction from the bandpass 10-15-year filtered 200-hPa geopotential height data and correlated it with GB precipitation (Fig. 2.5q). In observations, the negative ψ anomaly over the western US, which has shifted slightly more north than the BP 3-7-year map, extends out into the North Pacific in a zonal pattern. There is good agreement between the correlation patterns in Figs. 2.5q and 2.7u. The composite of the CCSM4 ensemble members captures the ψ dipole anomaly centered just off the west coast of North America, but the extension of the low pressure over the North Pacific is not apparent, reflecting underlying variability in the upstream pattern among the ensemble members (Fig. 2.5r). For example, members such as r2 (Fig. 2.5t) indicate that the CCSM4 captures the observed zonal upstream pattern given some specific initial conditions, but the diversity of patterns in other members suggests strong internal system variability that can affect GB precipitation (Deser et al., 2012, 2014).

2.3.4 Connectivity with the PDO

The correlation maps in Fig. 2.7 between bandpass 10-15-year filtered SSTs and GB precipitation depict a PDO-like pattern in the North Pacific. To examine further how models simulate the PDO modulation on the ENSO teleconnection, we assess PDO spatial patterns and the correlation between PDO and GB precipitation. We calculated the PDO Index for each model and observations following the approach described in section 2a. For each model, we chose the ensemble member that had the highest r_u value; over half of the models have ensemble members with r_u values at or above 0.8 (Fig. 2.3c), indicating a good performance in the depiction of PDO. (It is interesting to note the increased number of ensemble members that have maps with lower r_u values, with some nearing 0.) Contemporaneously, the correlation between the PDO Index and bandpass 10-15-year filtered GB precipitation is highly variable across the ensemble members (Fig. 2.3f). CCSM4, which has the best spatial pattern match (higher r_u; Fig. 2.3b), also has the closest correlation coefficient to observations, although the variance of the PDO and precipitation in that ensemble member is much higher than observations (Fig. 2.4b,e).

The correlation between the PDO Index and GB precipitation is maximized at a lag of about two years for observations (Fig. 2.3g). As previously mentioned, such phase lag is due to the teleconnection that emerges during the PDO transitions. However, only some models capture this lagged correlation (Fig. 2.3g) even though most have realistic PDO spatial patterns (Fig. 2.3c). MIROC5, HadGEM2-ES, and CCSM4, the models with the highest r_u values in Fig. 2.3c, have correlations

much lower than that of observations at a 2-year lag. However, some of the other models with r_u values above 0.8 have correlations near that of observations. Some of the models with the lower correlation coefficients in Fig. 2.3g have PDO Index variances that are much higher than the models with the higher correlation coefficients (compare Figs. 2.3g and 2.4f). Visual inspection of the PDO time series shows that the models with the near-zero correlation coefficients and higher variance (i.e. CCSM4, NorESM1-M, and CESM1(CAM5)) have more extreme (high amplitude) PDO fluctuations than those found in observations and in models with higher correlation coefficients and lower variance (i.e. MPI-ESM-LR). Additionally, the variance in the low-pass 7-year filtered GB precipitation (Fig. 2.4c) is higher in the models than in observations, and it tends to decrease in models with more realistic PDO spatial patterns (r_u, Fig. 2.3c).

2.3.5 Lagged relationship between Pacific QDO and GB precipitation

As noted in the Introduction, Wang et al. (2011) described the dynamical connection between the transition phase coupling of the Pacific QDO with GB precipitation. An atmospheric wave train sets up from the western tropical Pacific, where SST anomalies appear more strongly than the Niño-4 region during the transition, in an arc towards western North America. In order to show the model representation of this transition-phase teleconnection, we used the bandpass 10-15-year filtered data to compute correlations with GB precipitation lagging Pacific SSTs by three years, as shown in Fig. 2.8. The spatial patterns of these correlations are notably variable

(recall that we show only the ensemble member best matching the observed pattern). The area-weighted uncentered spatial correlations decrease rapidly across the models and even become negative in some models, indicating only a weak presence of the QDO transition dynamics in CMIP5 (Fig. 2.3d). For example, one ensemble member of CCSM4 has the highest pattern match in Fig. 2.3d (shaded bar), yet other members of CCSM4 have maps that are opposite in sign to observed patterns (x symbols below zero in Fig. 2.3d). Generally, as the area-weighted uncentered spatial correlations decrease and become negative, the correlation between Niño-4 SSTs and GB precipitation also decreases and becomes negative (Fig. 2.3h), suggesting that poor simulations of the Pacific QDO lead to even poorer simulations of its teleconnection impact on GB precipitation. Among all models, CCSM4 stands out as it captures both the spatial pattern of this transition-phase teleconnection (Fig. 2.8c) as well as the contemporaneous relationship between Niño-4 SSTs (where the Pacific QDO manifests itself) and GB precipitation (Fig. 2.3h).

2.4 Summary

This study focuses on determining the degree to which CMIP5 models are able to simulate observed interannual to multidecadal connections between Pacific SSTs and Great Basin precipitation. All of the models performed reasonably well on the interannual time scale as far as capturing ENSO; however, not all of the models produced the observed connection between Niño-4 SSTs and precipitation in the Great Basin. This discrepancy could be due to the phase of PDO present, as PDO

can alter the effect of ENSO on the Great Basin. Most models have a clear PDO signature, but the highly variable correlations between the simulated PDO Index and GB precipitation are likely due to the overly strong variance in the simulated PDO. For some of the models, the excessively strong correlations between bandpass 3-7-year SSTs and GB precipitation could be because the PDO did not appear to modulate ENSO at all. In contrast, the quasi-decadal connection (i.e. a dominant mode in the GB) proved to be more difficult for the models to capture. The lagged connection between Niño-4 SSTs and GB precipitation, and therefore, the transition phase of the Pacific QDO as discussed in Wang et al. (2010) and Wang et al. (2011), proves to be a challenge for the models.

Table 2.1. List of CMIP5 models used in this study, the number of ensemble members per model (denoted by #), and their corresponding institutions.

Model	#	*Institution*	*Reference*
ACCESS1.3	1	Commonwealth Scientific and Industrial Research Organization, Australia and Bureau of Meteorology, Australia (CSIRO-BOM)	Bi et al. (2013)
BCC-CSM1.1	3	Beijing Climate Center, China Meteorological Administration (BCC)	Xin et al. (2013)
CCSM4	6	National Center for Atmospheric Research (NCAR)	Gent et al. (2011)
CESM1(CAM5), CESM1(CAM5.1, FV2)	3, 4	National Science Foundation, Department of Energy, National Center for Atmospheric Research (NSF-DOE-NCAR)	Hurrell et al. (2013)
GFDL-CM3, GFDL-ESM2G	5, 1	Geophysical Fluid Dynamics Laboratory (NOAA GFDL)	Donner et al. (2011); Dunne et al. (2012)
GISS-E2-H, GISS-E2-R	5, 6	NASA Goddard Institute for Space Studies (NASA GISS)	Schmidt et al. (2014)
HadCM3, HadGEM2-CC, HadGEM2-ES	10, 1, 4	Met Office Hadley Centre, UK (MOHC)	Collins et al. (2001); Collins et al. (2011); Martin et al. (2011)
HadGEM2-AO	1	Met Office Hadley Centre, UK (MOHC); National Institute of Meteorological Research/Korea Meteorological Administration (NIMR/KMA)	Martin et al. (2011)
INM-CM4	1	Institute for Numerical Mathematics, Russian Academy of Sciences (INM)	Volodin et al. (2010)
IPSL-CM5A-LR	5	Institut Pierre-Simon Laplace, France (IPSL)	Mignot and Bony (2013)
MIROC5	4	Atmosphere and Ocean Research Institute (The University of Tokyo), National Institute for Environmental Studies, and Japan Agency for Marine-Earth Science and Technology	Watanabe et al. (2010)
MPI-ESM-LR, MPI-ESM-P	3, 2	Max Planck Institute for Meteorology, Germany (MPI-M)	Giorgetta et al. (2013)
MRI-CGCM3	3	Meteorological Research Institute, Japan (MRI)	Yukimoto et al. (2012)
NorESM1-M	3	Norwegian Climate Centre (NCC)	Bentsen et al. (2013)

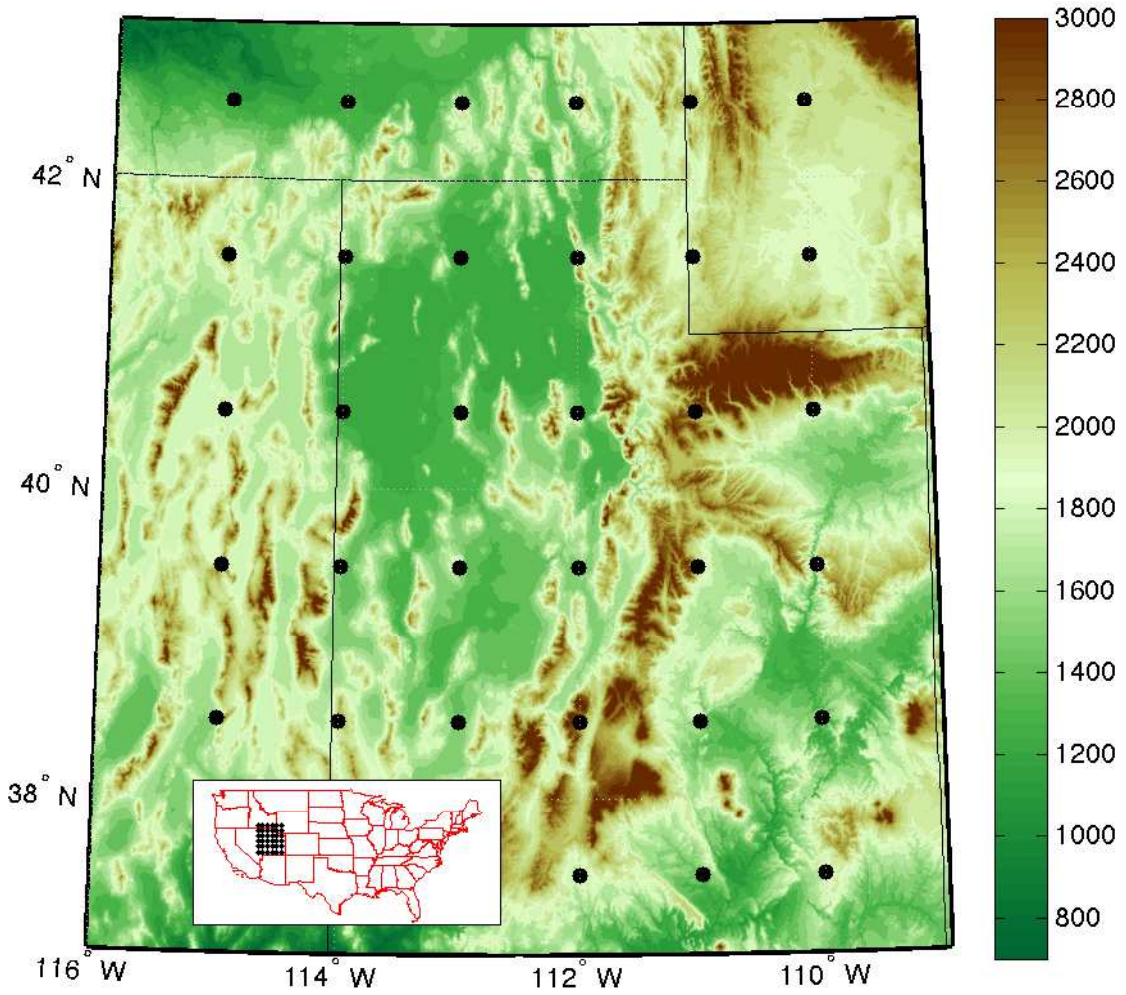

Fig. 2.1. The portion of the Great Basin used in the study (37.5-42.5°N and 115-110°W). The filled circles indicate the points in the GPCC precipitation dataset that were spatially averaged for analysis. Inset map shows location of region in the contiguous US. The colorbar indicates elevation in meters above sea level.

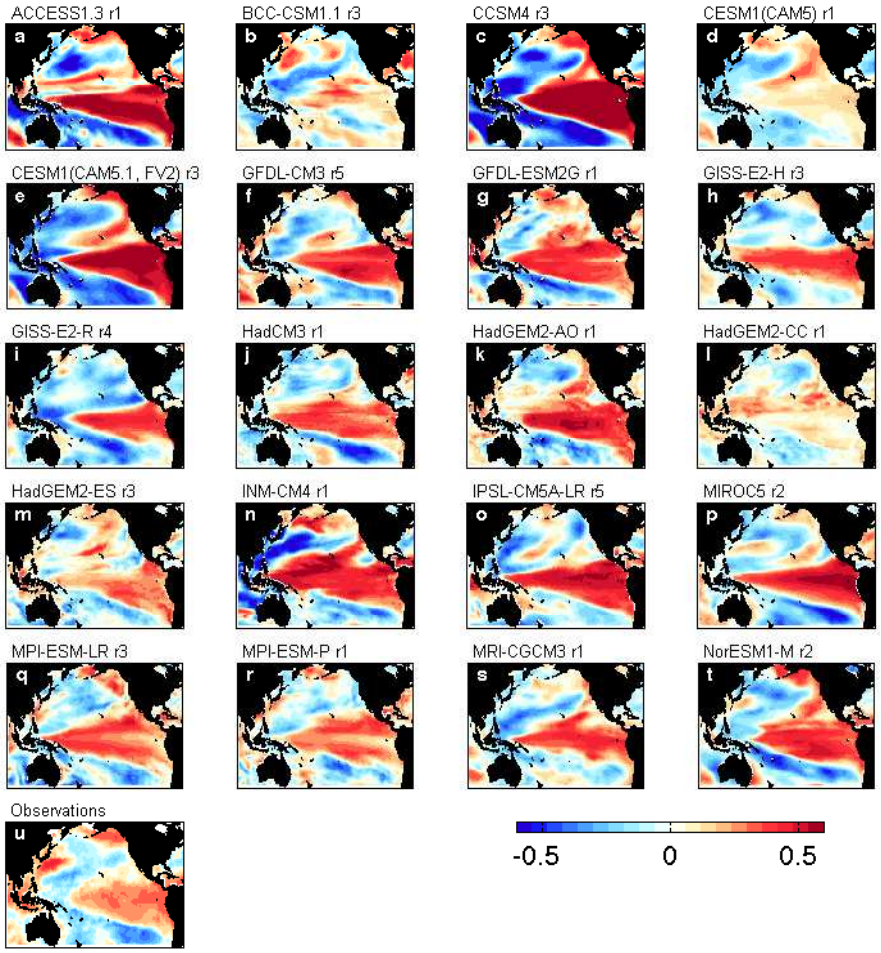

Fig. 2.2. Contemporaneous correlation maps between bandpass filtered 3-7 year SSTs and Great Basin precipitation. The model's ensemble member with the map that most closely matches that of the observations (panel u) is shown (match assessed using the area-weighted uncentered spatial correlation r_u; recall eq. 2.1).

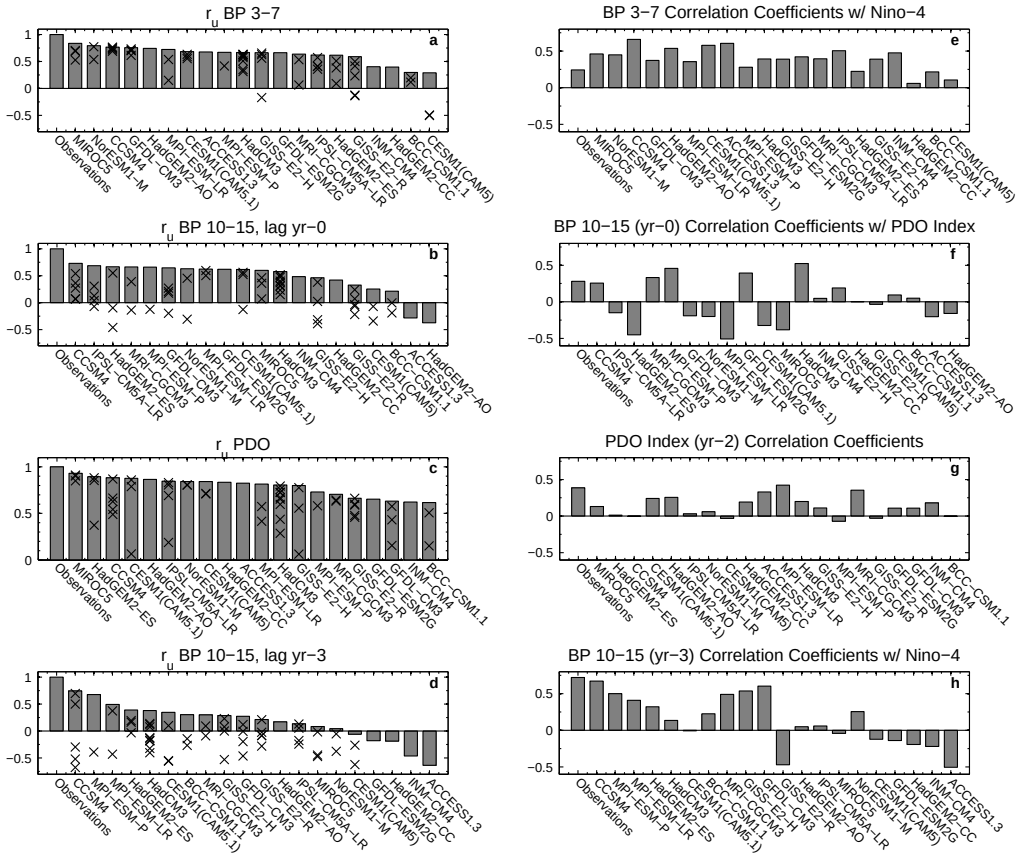

Fig. 2.3. Bar charts on the left show how well CMIP5 ensemble members capture observed spatial patterns related to Great Basin precipitation (P) and Pacific sea surface temperatures (SSTs), where the statistic used is the area-weighted uncentered spatial correlation (r_u, eq. 2.1). The ensemble member closest to observations is indicated by the bar, and other available ensemble members are indicated by the symbol x. The compared spatial patterns are: (a) correlation between P and SSTs for bandpass 3-7 years (i.e. maps in Fig. 2.2), (b) correlation between P and SSTs for bandpass 10-15 years (i.e. maps in Fig. 2.7), (c) the loading pattern (EOF) defining the Pacific Decadal Oscillation (maps not shown), and (d) correlation between P and SSTs for bandpass 10-15 years with SSTs leading P by 3 years (i.e. maps in Fig. 2.8). Bar charts on the right report correlation coefficients for (e) P and Niño-4 SST for bandpass 3-7 years, (f) PDO and bandpass 10-15 year P, (g) PDO and low-pass 7-year P with PDO leading P by 2 years, and (h) P and Niño-4 SST for bandpass 10-15 years with SST leading P by 3 years based on the transition-phase teleconnection. Each row orders the models according to the r_u values in the left panel of the row.

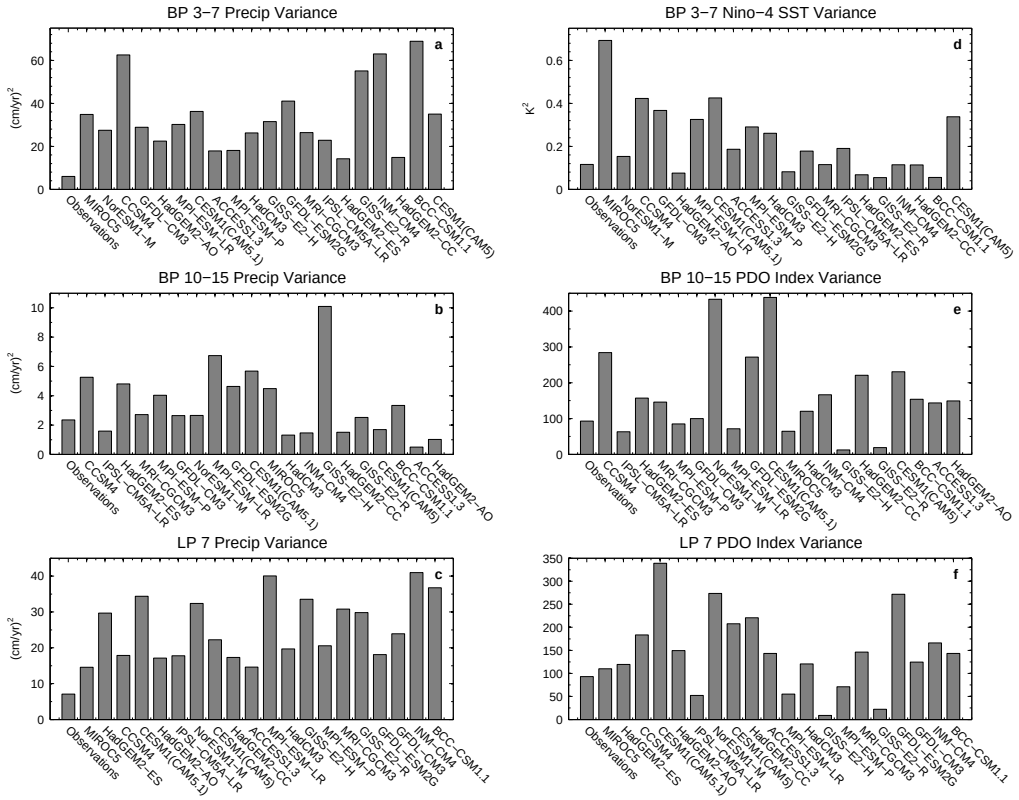

Fig. 2.4. Bar charts on the left show the Great Basin precipitation variance for (a) bandpass 3-7-year filtered data, (b) bandpass 10-15-year filtered data, and (c) low-pass 7-year data. Bar charts on the right show the variance of (d) bandpass 3-7-year Niño-4 SSTs, (e) the PDO Index of the ensemble members in panel b, and (f) the PDO Index of the ensemble members in panel c. Note that the order of the models here follows the first three rows in Fig. 2.3.

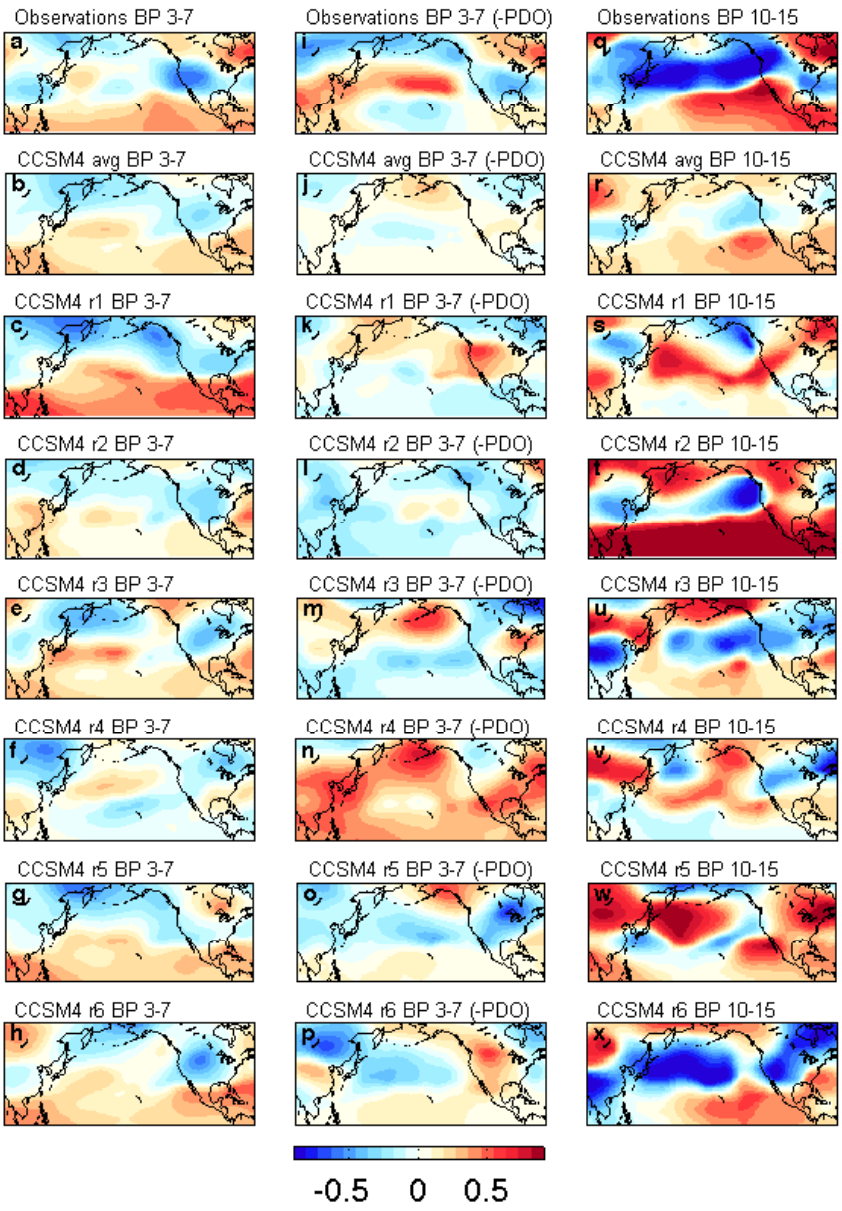

Fig. 2.5. Correlation maps between the bandpass 3-7-year filtered (a-h) and bandpass 10-15-year filtered (q-x) streamfunction and Great Basin precipitation for the observations, the average of all six ensemble members of CCSM4, and each individual ensemble member. The middle column (i-p) shows the streamfunction for the bandpass 3-7-year filtered data for only the years of negative PDO.

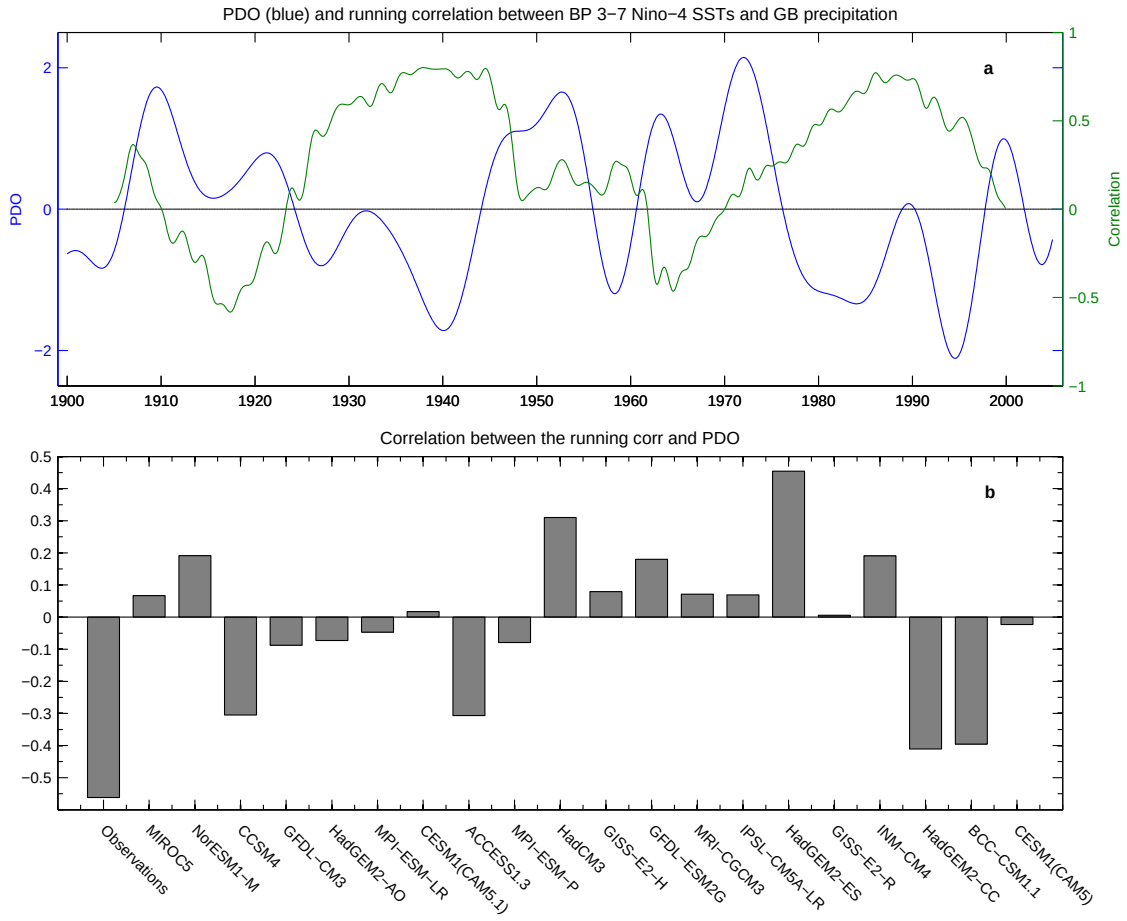

Fig. 2.6. PDO modulation of ENSO-driven precipitation. (a) For observations, the blue curve shows the Pacific Decadal Oscillation (PDO) Index and the green curve shows the 10-year running correlation between bandpass 3-7-year filtered Niño-4 SSTs and Great Basin precipitation (r_{EG}). (b) Correlation between the PDO Index and r_{EG} for observations and CMIP5 models. The order follows that of Fig. 2.3a,e.

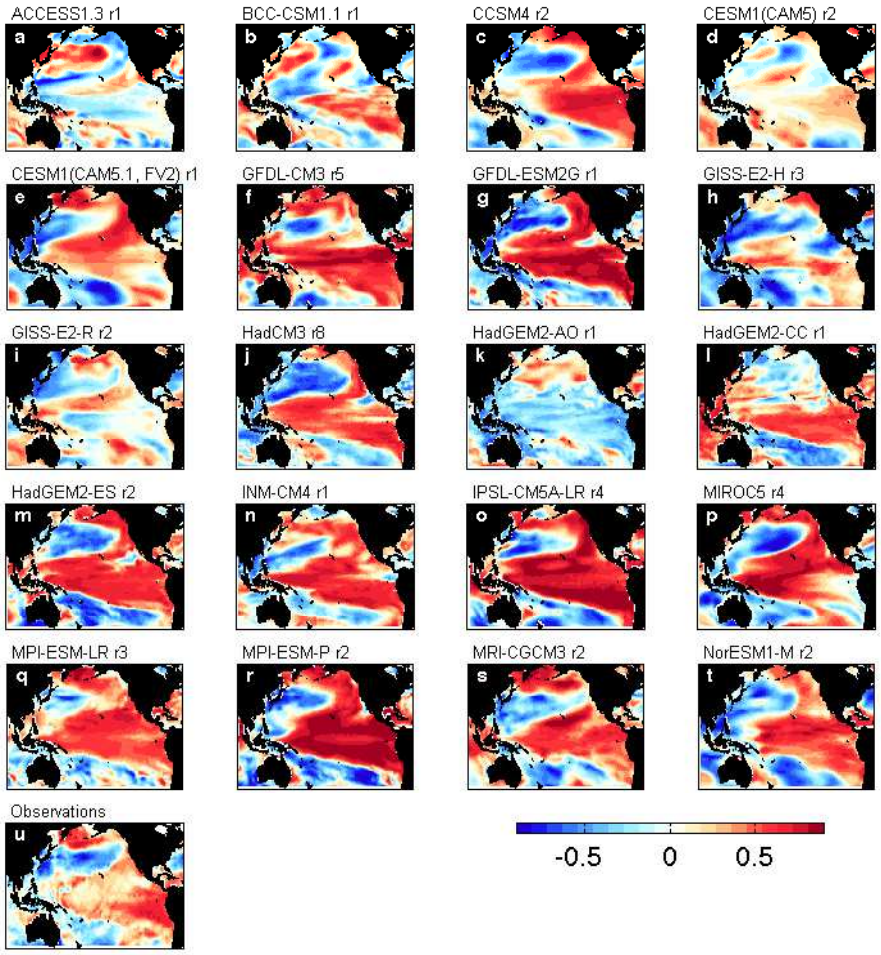

Fig. 2.7. Contemporaneous correlation maps between bandpass 10-15-year filtered SSTs and Great Basin precipitation. The model's ensemble member with the map that most closely matches that of the observations (panel u) is shown.

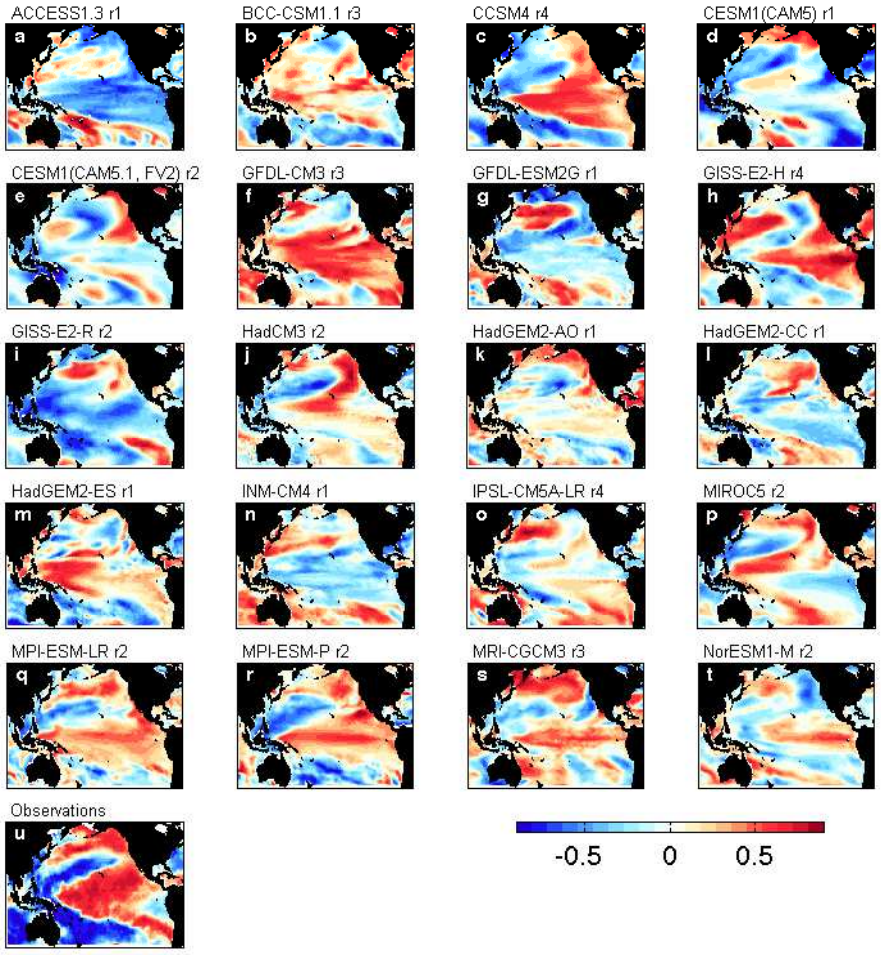

Fig. 2.8. Lagged correlation maps between bandpass 10-15-year filtered SSTs and Great Basin precipitation with precipitation lagging SSTs by 3 years. The model's ensemble member with the map that most closely matches that of the observations (panel u) is shown.

CHAPTER 3

MODEL ASSESSMENT FOR THE FUTURE

3.1 Introduction

The highly variable precipitation in the Great Basin and western US as a whole as discussed in previous chapters implies an uncertain future. As described in Chapter 2, an assessment of 20 CMIP5 models was completed to determine which models exhibited the most realistic connections between Pacific Ocean SST variability and Great Basin precipitation on interannual to multidecadal timescales. All of the timescales included in the analysis play a major role in creating the atmospheric patterns which result in precipitation in the Great Basin. Because all of the models performed favorably on the multidecadal timescale (i.e. PDO), the models were ranked based on their correlation maps on an interannual timescale (i.e. ENSO) and a quasi-decadal timescale (related to the Pacific QDO).

Using the results from the assessment, this study analyzes future precipitation data under a high emissions scenario (RCP 8.5) to determine what the future could potentially look like over the western US depending on which model is chosen. In addition, the results are used to force a nonstationary, daily stochastic weather

generator (Richardson, 1981; Wilks, 1999b; Woolhiser, 2008; Wilks, 2009). The stochastic weather generator takes the inputs from the results and generates a daily time series consisting of precipitation occurrence for a given time period. The stochastic weather generator is an important and useful tool for climate scientists, hydrologists, biologists, engineers, and planners alike. Continued work with the simulator involves resolving precipitation amount and simulating air temperature based on precipitation occurrence.

3.2 Data and Methods

3.2.1 Data

For the study presented in Chapter 2, twenty CMIP5 models satisfied the requirement of having the all-forcing historical precipitation output and sea surface temperature output, both back to at least 1900. To apply the results of that study to an analysis of future data, we obtained precipitation and SST data for future emissions scenario RCP 8.5 (high emissions) for all CMIP5 models in which it was available out to year 2099. The models that did not have RCP 8.5 data out to year 2099 and were eliminated were HadCM3 and MPI-ESM-P.

The data used in the stochastic weather generator portion of this study are 0.125° daily precipitation output from the CMIP5 run of the CCSM4 model. The data were calculated using the bias-correction constructed analogs (BCCA) method developed by (Maurer and Hidalgo, 2008) and extended from 1950 through 2100. The analysis domain for this portion of the study is the same domain used in 2: the eastern Great

Basin (37.5-42.5°N and 115-110°W). Two sites from within the domain – a point from the Wasatch Mountains, near Alta, and a point from the Salt Lake Valley – were selected for further analysis and comparison.

3.2.2 Methods

Using the results presented in Chapter 2 and as mentioned in the Introduction, a combined ranking of the interannual and quasi-decadal maps (Fig. 2.3a-b) determined the top performing CMIP5 models overall out of the twenty included in the first analysis. The ranking for the multidecadal timescale was not included in the combined ranking because all of the models performed favorably. Using the future data, the difference in mean precipitation between a late future 30-year period (2070-2099) and a historical 30-year period (1976-2005) was calculated over the western US. Over the same region and using the same time periods, the annual precipitation variance ratios were also computed.

The stochastic weather generator was used to model precipitation occurrence by employing a second-order Markov chain process, meaning the probability of observing a dry (or wet) day depends on the sequence of wet or dry conditions on the previous two days. For a given location, we use y_t to denote the precipitation amount on day t, where $t = 1, 2, ..., 365Y$ and Y indicates the number of years. The indicator variable

$$X_t = \begin{cases} 1, & \text{if } y_t > h; \\ 0, & \text{otherwise} \end{cases} \tag{3.1}$$

takes the value 1 to indicate a wet day (precipitation of at least $h = 0.25$ mm) and

takes the value of 0 to indicate a dry day. The probability of observing a wet or dry day in the second-order Markov chain framework follows as

$$p_{ij0}(t) = P\{X_t = 0|X_{t-1} = j|X_{t-2} = i\}; i, j = 0, 1; t = 1, 2, ..., 365Y. \tag{3.2}$$

Equation 3.2 represents four probabilities (one for each of the possible sequences of wet or dry on days t – 1 and t – 2). For example, $p_{010}(t)$ denotes the probability of observing the sequence dry-wet-dry completing on day t. The four remaining p terms represent the probability of observing a wet day following a given sequence of wet or dry and are given by $p_{ij1}(t) = 1 - p_{ij0}(t)$.

The likelihood of observing a particular sequence of X_t is given by the Bernoulli measure

$$L = \prod_{i,j=0}^{1} \prod_{t=1}^{365Y} p_{ijo}(t)^{b_{ijo}(t)}[1 - p_{ijo}(t)]^{b_{ij1}(t)} \tag{3.3}$$

where

$$b_{ijk}(t) = \begin{cases} 1, & \text{if } X_{t-2} = i,\ X_{t-1} = j,\ X_t = k; \\ 0, & \text{otherwise} \end{cases} \tag{3.4}$$

The system is first estimated assuming cyclostationarity. Then, we assess the increase in likelihood when degrees of freedom are added to account for nonstationarity introduced by climate change or low-frequency oceanic modes of variability.

Usually, the Markov chain process is applied assuming stationarity. Cyclostationarity indicates that the p_{ij0} terms are periodic, meaning $p_{ij0}(t+K365)=p_{ij0}(t)$ for any integer K. We can then rewrite the product over t in eq. 3.3 as a product over day of year n

$$L = \prod_{i,j=0}^{1} \prod_{n=1}^{365} p_{ijo}(n)^{N_{ijo}(n)}[1 - p_{ijo}(n)]^{N_{ij1}(n)} \tag{3.5}$$

where N_{ijk} is the number of times that the sequence $\{X_{t-2}=i, X_{t-1}=j, X_t=k\}$ occurred on day of year n. We seek to maximize L in order to determine estimates for the parameters that will give the most probable results when put through the weather generator. We accomplish this with a Newton-Raphson iterative process.

However, due to the effects of climate change and modes of variability associated with the Pacific Ocean, it is important to assess the importance of nonstationarity. We introduce perturbed versions of the p terms, including one for climate change, one for the effects of the ENSO mode, and one for the quasi-decadal effects. In addition, since the study spans multiple sites over the eastern Great Basin, we created a multisite weather generator. Following Wilks (2009), we generalize the precipitation occurrence process to an arbitrary number of sites, and after calculating each site individually, we use the brute force iterative process presented in Brissette et al. (2007) so the synthetic correlation matrix best matches the observed correlation matrix over the arbitrary number of sites.

3.3 Results

3.3.1 Future changes in precipitation under a high emissions scenario

The difference in the mean precipitation between a late future period (2070-2099) and a historical period (1976-2005) was calculated over the western US (Fig. 3.1). We ranked the models based on the sum of the rankings in Fig. 2.3a and Fig. 2.3b from Chapter 2 and show the top 10 models individually (Fig. 3.1a-j). It is obvious in Fig. 3.1 that each of the top ten performing models have very different realizations

for mean precipitation over the western US. The difference between the composite of the top ten models and all models with future data is small; however, it may be more beneficial to consider a composite of the top three or top five models because of the reduction of different patterns. The location of the zero-line reflects how the PDO modulation of ENSO can have quite different effects on precipitation in the GB. In general, the mean precipitation increases over the northwestern US and decreases over the southwestern US. The decrease over the southwestern US could indicate a weakening of the monsoon; however, the composite of all models (Fig. 3.1l) does not weaken the monsoon as much as the composite of the top 10 models (Fig. 3.1k), as shown in Fig. 3.1m. The mean precipitation change over the GB depends on the model; some models increase mean precipitation (i.e. MRI-CGCM3 and GFDL-ESM2G) while others decrease mean precipitation (see Fig. 3.1n). For the top 10 models (Fig. 3.1k) and all models together (Fig. 3.1l), the zero-line is located centrally over the GB, with a mean increase of about 2-3 cm per year in the model composites (Fig. 3.1n).

The annual precipitation variance ratios over the western US were also determined, using the same future and historical periods as mentioned previously (Fig. 3.2). In general, the models showing regions with an increase in mean precipitation as seen in Fig. 3.1 also show an increase in variance. The models tend to decrease the variance in areas over the southwestern US where the mean precipitation decreases. However, the composite of all models increases the variance over the southwest compared to the composite of the top 10 models (Fig. 3.2m). Both model composites

[the top 10 (Fig. 3.2k) and full set (Fig. 3.2l)] increase the variance over the GB by about 50 percent (red lines; Fig. 3.2n). Fig. 3.2m highlights how the composite of all models increases the variance over the southern portion of the GB while decreasing the variance over the northern portion of the GB relative to the top 10 models, further emphasizing the difficultly in predicting future changes in this region. The north-south dipole structure reflected in Fig. 3.2m resembles the canonical ENSO or PDO pattern (e.g. Mantua et al., 1997), and this seems in agreement with the ability of the top 10 models to capture the PDO teleconnection in comparison to the rest of the models (recall Fig. 2.3).

3.3.2 Stochastically simulating precipitation occurrence

Fig. 3.3 shows the probability of precipitation occurring on each day over a year given any combination of previous wet or dry days for both a Salt Lake Valley site and a site near Alta in the Wasatch Mountain Range. For both sites, the probability of precipitation occurring after two dry days is the relatively low, while the probability of precipitation occurring after two wet days is relatively high. The probabilities for the Salt Lake Valley site show a typical spring and fall maxima, lower probabilities in the winter, and a minimum in the summer (Fig. 3.3a). The probabilities for the Alta site are overall higher than the probabilities for the Salt Lake Valley site, which is consistent with its tendency to receive orographic enhancement of precipitation. However, it is interesting to note that the maxima and minima for Alta are similar to that of the valley (Fig. 3.3b).

Nonstationary perturbations were added to the stochastic weather generator in the form of a trend, high-frequency oceanic variability due to an ENSO-like mode, and low-frequency variability due to a quasi-decadal, PDO-like mode. Fig. 3.4 displays the results of adding the nonstationarity for the probability of precipitation occurring following a wet-dry sequence for the Alta site. The top panel shows a complete perturbed time series of annually averaged probabilities from 1950-2100; the trend is clearly visible, and the amplitude of the series varies markedly from year to year in some places, especially around 1965 and 1985. The bottom panel displays the perturbed monthly time series against the cyclostationary monthly time series for 1985-1990. The perturbations create greater fluctuations than just the annual cycle, and these fluctuations vary quite a bit over a relatively short amount of time. It was necessary to add nonstationarity because of the effect climate change and oceanic modes have on GB precipitation, as made clear by this figure.

Using the downscaled CCSM4 data, stochastic synthetic data were created. A scatter plot of the probability of precipitation per month for the Salt Lake Valley site was made in order to compare the model data to the simulated data and determine if the stochastic weather generator correctly simulated the model data (Fig. 3.5). Ten 3-year simulations were completed and plotted (red pluses, Fig. 3.5) to show the high variability when computing short-term simulations. Short-term simulations can result in especially dry or wet series of months, whereas longer term simulations better match the sequences of the model data. A single 56-year simulation (black filled circles, Fig. 3.5) more closely matches that of the model data than a random

3-year simulation. Even though the simulations have the same statistical properties as the model data, for shorter simulations, the stochastic weather generator produces realizations that differ markedly from the expected value of the observations.

3.4 Summary

Using the results presented in Chapter 2, the 20 CMIP5 models were ranked according to their performance in capturing the connectivity between GB precipitation and Pacific Ocean variability on the interannual and quasi-decadal time scales. Future precipitation data were obtained for all models in which it was available, and the mean precipitation between a late future period (2070-2099) and a historical period (1976-2005) was computed over the western US. In general, the models predict the northern half of the western US to be wetter while the southern half of the western US will be dryer, with the eastern GB situated somewhere in between. The top 10 models show major differences in how the mean precipitation will change and greatly vary in where the zero-line is located, highlighting the difficultly in predicting these changes over the GB. The precipitation variance ratio over the same time period and area was also computed. The results follow that of the mean precipitation results; for the most part, the variance ratio is shown to increase over areas where the mean precipitation increases and vice versa.

Based on the ranking of the models, CCSM4 is the top performing model of the 20 that were previously evaluated. Downscaled CCSM4 historical and future high emissions (RCP 8.5) precipitation data were obtained to force a nonstationary, daily

stochastic weather generator based largely on the work of Brissette et al. (2007), Woolhiser (2008), and Wilks (2009). The stochastic weather generator employs a two-state, second-order Markov chain process to determine precipitation occurence, and modifications were made to introduce nonstationarity from the interannual and quasi-decadal oceanic modes and to generalize over multiple sites. The probabilities of precipitation for two sites–one near Alta in the Wasatch Mountains and one in the Salt Lake Valley–were analyzed over annual and longer timescales to determine how well the stochastic weather generator can simulate modeled precipitation. It was shown that nonstationarity is especially important to consider because of the effects of the different Pacific Ocean modes of variability on GB precipitation. The stochastic weather generator also performs better when simulating long-term realizations because of high variability in short-term realizations.

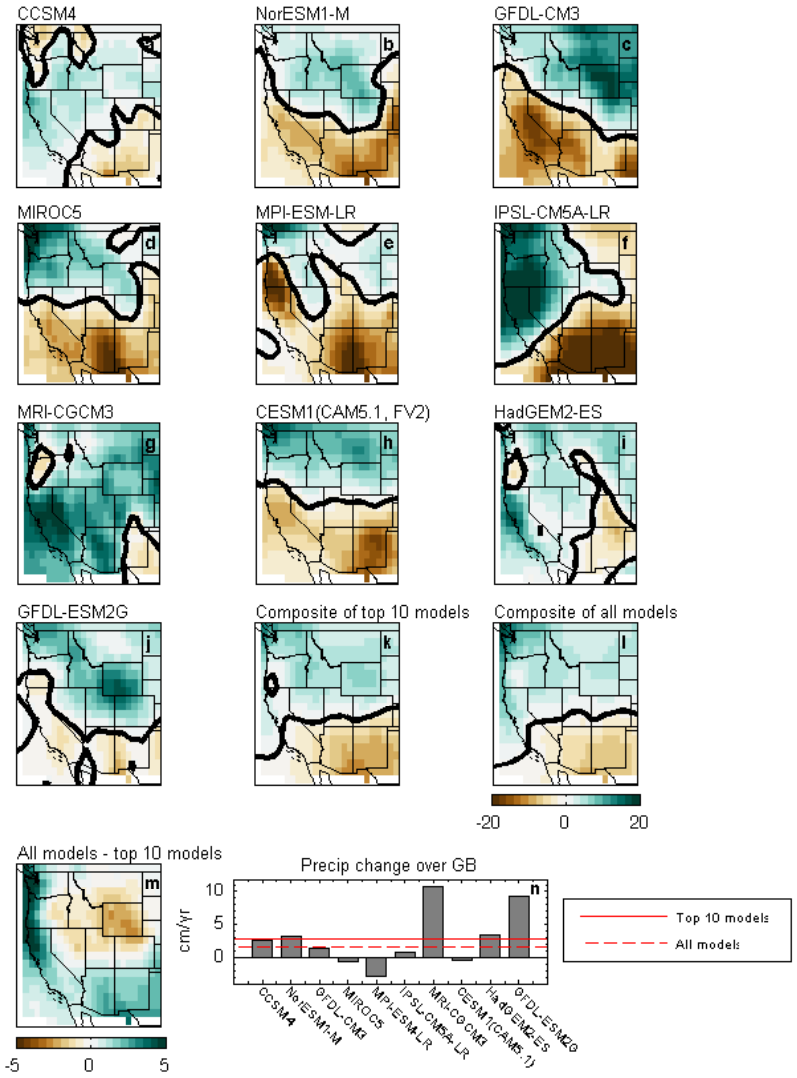

Fig. 3.1. The change in the mean precipitation between a future period (2070-2099) and a historical period (1976-2005) based on a high emissions scenario (RCP 8.5). Maps are shown for each of the top 10 models (panels a-j), the composite of the top 10 models (panel k), the composite of all models (panel l), and the difference between the composites (panel m). The zero contour is bold. The bar chart (panel n) shows the spatially averaged mean precipitation change over the GB for each of the top 10 models and the composites. The order of the models is based on the sum of the model rankings in Fig. 2.3a-b.

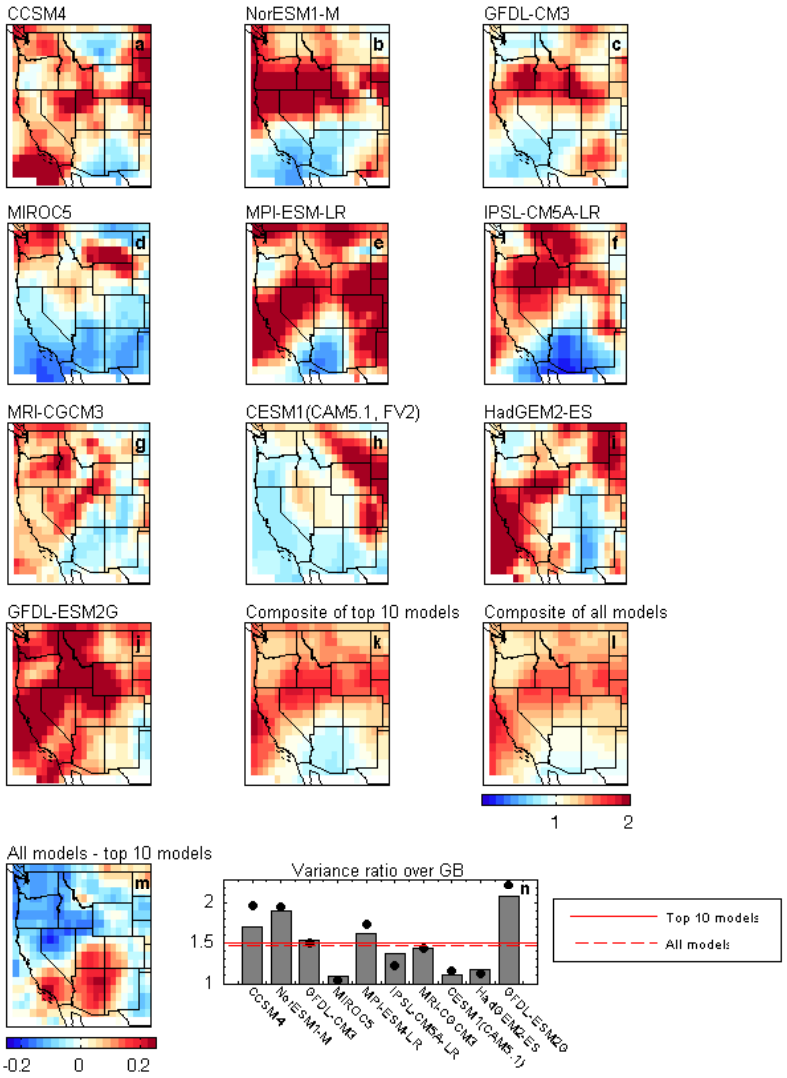

Fig. 3.2. The precipitation variance ratio between a future period (2070-2099) and a historical period (1976-2005) based on a high emissions scenario (RCP 8.5). Maps are shown for each of the top 10 models (panels a-j), the composite of the top 10 models (panel k), the composite of all models (panel l), and the difference between the composites (panel m). The bar chart (panel n) shows the spatially averaged variance ratios over the GB for each of the top 10 models and the composites. The filled black circles in panel n indicate the variance ratios computed after spatially averaging over the GB. The order of the models follows that of Fig. 3.1.

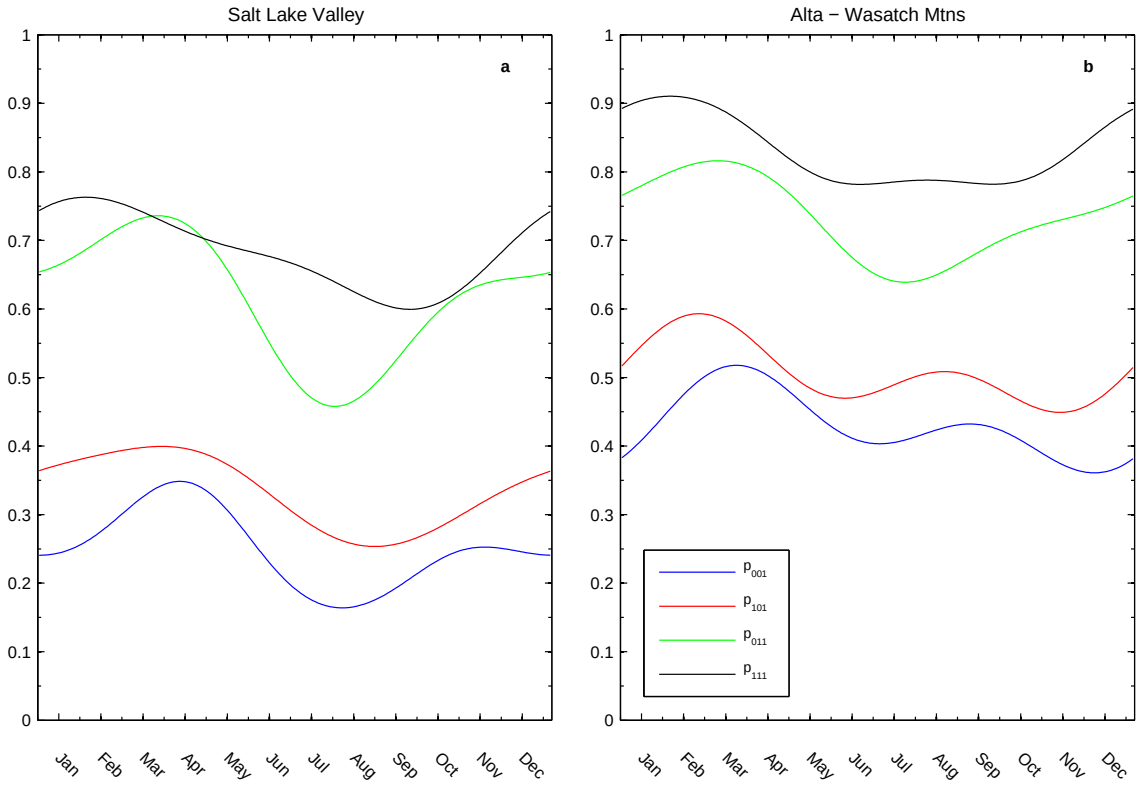

Fig. 3.3. Probability of precipitation occurrence on any given day of the year for (a) a site in the Salt Lake Valley and (b) a site in the approximate location of Alta in the Wasatch Mountain Range.

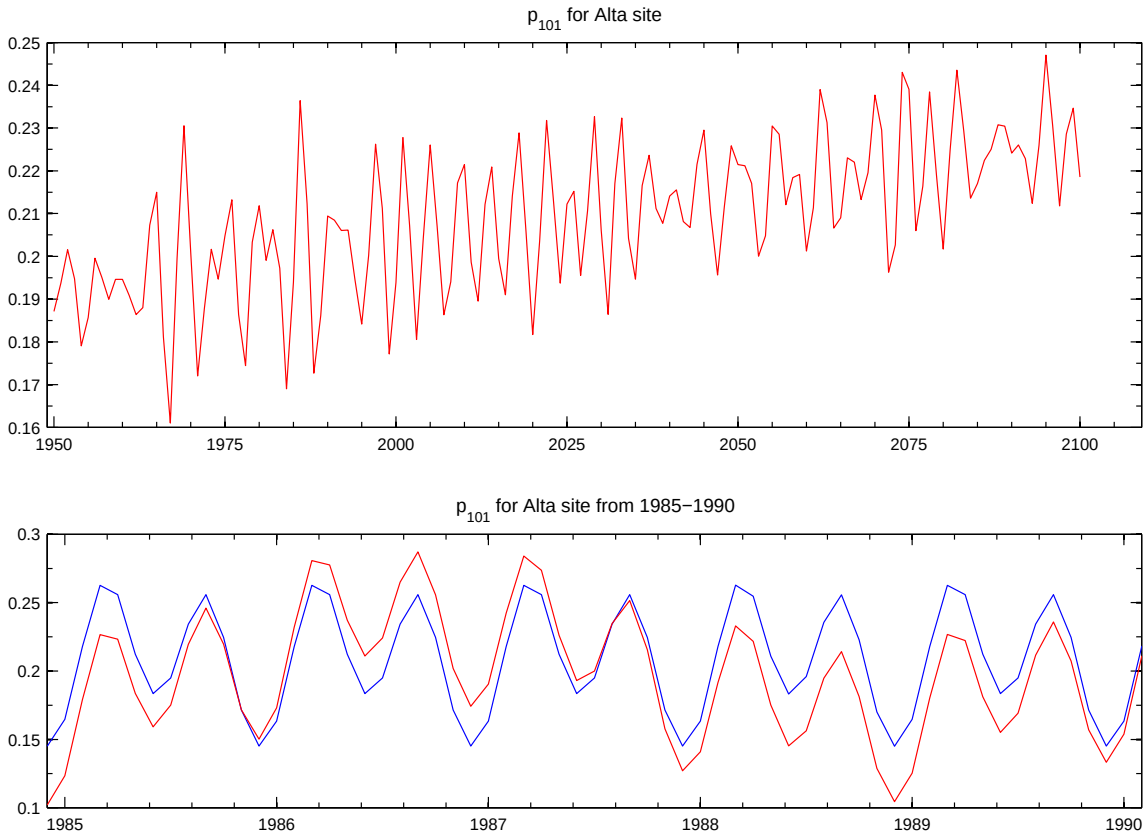

Fig. 3.4. The top panel shows the perturbed annually averaged time series of p_{101} for the Alta site for the years 1950-2100. The bottom panel shows the same time series and the cyclostationary time series zoomed in over years 1985-1990 to show how much of an effect the perturbations from the oceanic modes have on the probability.

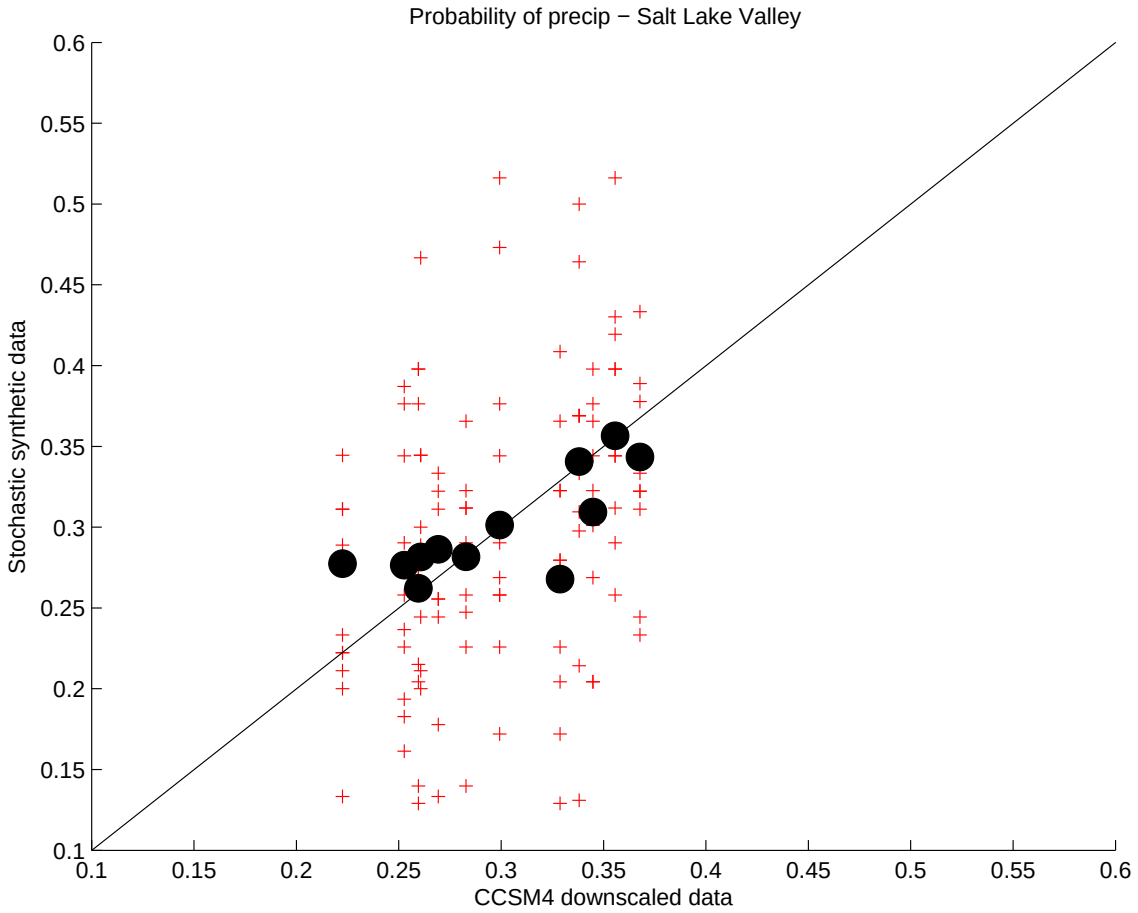

Fig. 3.5. Scatter plot of the probability of precipitation per month for the Salt Lake Valley. The red crosses indicate 3-year simulations of synthetic data, and there are ten different 3-year simulations shown to highlight variability. The black filled circles indicate one 56-year simulation; note how the dots are more clustered around the 1:1 line.

CHAPTER 4

DISCUSSION AND CONCLUSIONS

Of the twenty models evaluated, CCSM4 consistently produced at least one ensemble member that compared well with observations. CCSM4 had high r_u values for both the contemporaneous and 3-year lagged bandpass 10-15 year filtered data as well as the PDO. The only other model that simulated well all three variabilities more than once was MIROC5, which had an ensemble member with the highest spatial pattern match for the bandpass 3-7 year filtered contemporaneous correlation and PDO correlation. The high performance of CCSM4 at every time scale (discussed in DeFlorio et al., 2013) suggests that it might perform better than other models in the simulation of the Pacific SST–GB precipitation variability under increased greenhouse gas emissions.

For the most part, models with more than one ensemble member performed more favorably in the model assessment. The models with only one ensemble member (ACCESS1-3, GFDL-ESM2G, HadGEM2-AO, HadGEM2-CC, and INM-CM4) had only one opportunity to capture the connection between Pacific SST variability and GB precipitation while models with more than one ensemble member had a better chance to cover the full spectrum of internal variability. While this observation

echoes other studies (e.g. Kirtman and Shukla, 2002; He et al., 2014) regarding the advantage of "multimodel" ensembles, the implication from this study is that the connectivity between Pacific SSTs and GB precipitation is highly sensitive to the initial conditions, including the state of the Pacific Ocean. Even slight changes in the initial conditions can result in vastly different outcomes in terms of interannual and decadal variations (e.g. Deser et al., 2012, 2014). Additionally, at a lower resolution, the complex terrain of the Great Basin domain in this study is smoothed out and thus, precipitation values are likely underestimated (or overestimated) in some places.

At last, models generally fail to capture the life cycles of PDO and associated impacts on GB precipitation. This may result from the periodicity of PDO being incorrectly simulated or that the teleconnection associated with the PDO transition, which is much weaker in SST anomalies in the tropics, did not exhibit a correct pattern. However, using a 2,000-year simulation by GFDL-CM2.1, Wang et al. (2012) showed that long control runs are possible to depict the transition-phase effect of PDO on the GB precipitation. This aspect echoes the previous argument of models capturing the full spectrum of internal variability, but it nonetheless requires further investigation.

The first part of this study was able to identify the models that are most likely to capture the observed connectivity between GB precipitation and Pacific Ocean variability and are therefore most likely to reliably project future variations. The ranking of the models based on their pattern matching statistic for the high-frequency ENSO-like mode (BP 3-7 years, Fig. 2.3a) and their pattern matching statistic for

the low-frequency PDO-like mode (BP 10-15 years, Fig. 2.3b) resulted in CCSM4 being the top performing model. Even though there are many differences between the top models, the purpose of the ranking was to narrow down the models that should be considered when completing future analyses with a stochastic weather generator and dynamical downscaling to the one or ones that are best able to capture the ocean-precipitation connection, because it is simply too expensive to incorporate all of the models in the simulations.

Using the results of the first part of the study and following the model ranking, downscaled CCSM4 precipitation data from 1950 through 2100 were used to generate simulations for two sites within the GB with a daily, nonstationary stochastic weather generator. The probabilities of precipitation for the two sites, a site in the Salt Lake Valley and a site near Alta in the Wasatch Mountains, follow similar patterns throughout the year, but the probabilities of precipitation overall are increased for Alta. This increase is likely due to orographic enhancement. Even though they have similar patterns of the probability of precipitation occurrence, the two sites potentially exhibit differences in the patterns of precipitation amount due to their different elevations. Nonstationarity was added with SST time series generated with the CCSM4 data used in the first part of the study. The nonstationarity due to climate change and oceanic modes of variability result in a major difference in the probability of precipitation over a long time period, as seen in Fig. 3.4. Because of how the GB is affected by both climate change and the oceanic modes, it was important to consider those when generating synthetic precipitation data for use in

analyses into the future. Additionally, the length of a simulation proves to be an important consideration; short-term simulations have considerably more variability than long-term simulations because of the time needed for the stochastic weather generator to converge on the expected value of the model data. Initial conditions could also play a role in the short-term variability.

Downscaled WRF (Weather Research and Forcasting) model simulations are currently underway using the CCSM4 model as inputs because it exhibited the best connection between GB precipitation and the various Pacific Ocean modes of variability. In addition, future work includes working with stochastic realizations of precipitation amount and developing a nonstationary stochastic framework for air temperature based on precipitation occurrence.

REFERENCES

Alexander, L. V. and J. M. Arblaster, 2009: Assessing trends in observed and modelled climate extremes over Australia in relation to future projections. *International Journal of Climatology*, **29 (3)**, 417–435, doi:10.1002/joc.1730, URL http://dx.doi.org/10.1002/joc.1730.

Alexander, M. A., I. Bladé, M. Newman, J. R. Lanzante, N.-C. Lau, and J. D. Scott, 2002: The atmospheric bridge: The influence of ENSO teleconnections on air–sea interaction over the global oceans. *J. Climate*, **15 (16)**, 2205–2231, doi:10.1175/1520-0442(2002)015¡2205:TABTIO¿2.0.CO;2, URL http://dx.doi.org/10.1175/1520-0442(2002)015<2205:TABTIO>2.0.CO;2.

Ault, T. R., J. E. Cole, and S. St. George, 2012: The amplitude of decadal to multidecadal variability in precipitation simulated by state-of-the-art climate models. *Geophysical Research Letters*, **39 (21)**, n/a–n/a, doi:10.1029/2012GL053424, URL http://dx.doi.org/10.1029/2012GL053424.

Bailey, N. T. J., 1964: *The Elements of Stochastic Processes*. John Wiley, New York, p. 39 pp.

Bardsley, T., A. Wood, M. Hobbins, T. Kirkham, L. Briefer, J. Niermeyer, and S. Burian, 2013: Planning for an uncertain future: Climate change sensitivity assessment toward adaptation planning for public water supply. *Earth Interact.*, **17 (23)**, 1–26, doi:10.1175/2012EI000501.1, URL http://dx.doi.org/10.1175/2012EI000501.1.

Barnett, T. P., J. C. Adam, and D. P. Lettenmaier, 2005: Potential impacts of a warming climate on water availability in snow-dominated regions. *Nature*, **438 (7066)**, 303–309, URL http://dx.doi.org/10.1038/nature04141.

Bentsen, M., et al., 2013: The Norwegian Earth System Model, NorESM1-M – part 1: Description and basic evaluation of the physical climate. *Geoscientific Model Development*, **6 (3)**, 687–720, doi:10.5194/gmd-6-687-2013, URL http://www.geosci-model-dev.net/6/687/2013/.

Bi, D., et al., 2013: The ACCESS coupled model: description, control climate and evaluation. *Australian Meteorological and Oceanographic Journal*, **63**, 41–64.

Brekke, L., 24 April 2013: New CMIP5 downscaled climate projections. *11th Annual CPASW Climate Prediction Applications Science Workshop, Logan, UT*.

Brissette, F., M. Khalili, and R. Leconte, 2007: Efficient stochastic generation of multi-site synthetic precipitation data. *Journal of Hydrology*, **345 (3–4)**, 121 – 133, doi:http://dx.doi.org/10.1016/j.jhydrol.2007.06.035, URL http://www.sciencedirect.com/science/article/pii/S002216940700385X.

Brown, D. P., 2011: Winter circulation anomalies in the western United States associated with antecedent and decadal ENSO variability. *Earth Interact.*, **15 (3)**, 1–12, doi:10.1175/2010EI334.1, URL http://dx.doi.org/10.1175/2010EI334.1.

Collins, M., S. F. B. Tett, and C. Cooper, 2001: The internal climate variability of HadCM3, a version of the Hadley Centre coupled model without flux adjustments. *Climate Dynamics*, **17 (1)**, 61–81, doi:10.1007/s003820000094, URL http://dx.doi.org/10.1007/s003820000094.

Collins, W. J., et al., 2011: Development and evaluation of an earth-system model – HadGEM2. *Geoscientific Model Development*, **4 (4)**, 1051–1075, doi:10.5194/gmd-4-1051-2011, URL http://www.geosci-model-dev.net/4/1051/2011/.

Cook, E. R., C. A. Woodhouse, C. M. Eakin, D. M. Meko, and D. W. Stahle, 2004: Long-term aridity changes in the western united states. *Science*, **306 (5698)**, 1015–1018, doi:10.1126/science.1102586, URL http://www.sciencemag.org/content/306/5698/1015.abstract, http://www.sciencemag.org/content/306/5698/1015.full.pdf.

DeFlorio, M. J., D. W. Pierce, D. R. Cayan, and A. J. Miller, 2013: Western U.S. extreme precipitation events and their relation to ENSO and PDO in CCSM4. *J. Climate*, **26 (12)**, 4231–4243, doi:10.1175/JCLI-D-12-00257.1, URL http://dx.doi.org/10.1175/JCLI-D-12-00257.1.

Deser, C., R. Knutti, S. Solomon, and A. S. Phillips, 2012: Communication of the role of natural variability in future North American climate. *Nature Clim. Change*, **2 (11)**, 775–779, URL http://dx.doi.org/10.1038/nclimate1562.

Deser, C., A. S. Phillips, M. A. Alexander, and B. V. Smoliak, 2014: Projecting North American climate over the next 50 years: Uncertainty due to internal variability*. *J. Climate*, **27 (6)**, 2271–2296, doi:10.1175/JCLI-D-13-00451.1, URL http://dx.doi.org/10.1175/JCLI-D-13-00451.1.

Dettinger, M. D., D. R. Cayan, H. F. Diaz, and D. M. Meko, 1998: North–south precipitation patterns in western North America on interannual-to-decadal timescales. *J. Climate*, **11 (12)**, 3095–3111, doi:10.1175/1520-0442(1998)011¡3095:NSPPIW¿2.0.CO;2, URL http://dx.doi.org/10.1175/1520-0442(1998)011<3095:NSPPIW>2.0.CO;2.

Donner, L. J., et al., 2011: The dynamical core, physical parameterizations, and basic simulation characteristics of the atmospheric component AM3 of the GFDL Global Coupled Model CM3. *J. Climate*, **24 (13)**, 3484–3519, doi:10.1175/2011JCLI3955.1, URL http://dx.doi.org/10.1175/2011JCLI3955.1.

Dunne, J. P., et al., 2012: GFDL's ESM2 global coupled climate-carbon earth system models. part I: Physical formulation and baseline simulation characteristics. *J. Climate*, **25 (19)**, 6646–6665, doi:10.1175/JCLI-D-11-00560.1, URL http://dx.doi.org/10.1175/JCLI-D-11-00560.1.

Frankignoul, C., N. Sennéchael, Y.-O. Kwon, and M. A. Alexander, 2011: Influence of the meridional shifts of the Kuroshio and the Oyashio extensions on the atmospheric circulation. *J. Climate*, **24 (3)**, 762–777, doi:10.1175/2010JCLI3731.1, URL http://dx.doi.org/10.1175/2010JCLI3731.1.

Gent, P. R., et al., 2011: The Community Climate System Model version 4. *Journal of Climate*, **24**, 4973–4991, doi:10.1175/2011JCLI4083.1.

Gershunov, A. and T. P. Barnett, 1998: Interdecadal modulation of ENSO teleconnections. *Bull. Amer. Meteor. Soc.*, **79 (12)**, 2715–2725, doi:10.1175/1520-0477(1998)079¡2715:IMOET¿2.0.CO;2, URL http://dx.doi.org/10.1175/1520-0477(1998)079<2715:IMOET>2.0.CO;2.

Gershunov, A., T. P. Barnett, and D. R. Cayan, 1999: North Pacific interdecadal oscillation seen as factor in ENSO-related North American climate anomalies. *Eos, Transactions American Geophysical Union*, **80 (3)**, 25–30, doi:10.1029/99EO00019, URL http://dx.doi.org/10.1029/99EO00019.

Gill, A. E., 1980: Some simple solutions for heat-induced tropical circulation. *Quarterly Journal of the Royal Meteorological Society*, **106 (449)**, 447–462, doi:10.1002/qj.49710644905, URL http://dx.doi.org/10.1002/qj.49710644905.

Giorgetta, M. A., et al., 2013: Climate and carbon cycle changes from 1850 to 2100 in MPI-ESM simulations for the Coupled Model Intercomparison Project phase 5. *Journal of Advances in Modeling Earth Systems*, n/a–n/a, doi:10.1002/jame.20038, URL http://dx.doi.org/10.1002/jame.20038.

Guilyardi, E., A. Wittenberg, A. Fedorov, M. Collins, C. Wang, A. Capotondi, G. J. van Oldenborgh, and T. Stockdale, 2009: Understanding El Niño in ocean–atmosphere general circulation models: Progress and challenges. *Bull. Amer. Meteor. Soc.*, **90 (3)**, 325–340, doi:10.1175/2008BAMS2387.1, URL http://dx.doi.org/10.1175/2008BAMS2387.1.

Hamming, R., 1998: *Digital Filters*. 3d ed., Dover Publications, 296 pp. pp.

Hannachi, A., I. T. Jolliffe, and D. B. Stephenson, 2007: Empirical orthogonal functions and related techniques in atmospheric science: A review. *International Journal of Climatology*, **27 (9)**, 1119–1152, doi:10.1002/joc.1499, URL http://dx.doi.org/10.1002/joc.1499.

He, J., B. J. Soden, and B. Kirtman, 2014: The robustness of the atmospheric circulation and precipitation response to future anthropogenic surface warming. *Geophysical Research Letters*, **41 (7)**, 2614–2622, doi:10.1002/2014GL059435, URL http://dx.doi.org/10.1002/2014GL059435.

Hurrell, J. W., et al., 2013: The Community Earth System Model: A framework for collaborative research. *Bull. Amer. Meteor. Soc.*, –, doi:10.1175/BAMS-D-12-00121.1, URL http://dx.doi.org/10.1175/BAMS-D-12-00121.1.

Iacobucci, A. and A. Noullez, 2005: A frequency selective filter for short-length time series. *Computational Economics*, **25 (1-2)**, 75–102, doi:10.1007/s10614-005-6276-7, URL http://dx.doi.org/10.1007/s10614-005-6276-7.

IPCC, 2013: *Working Group I Contribution to the IPCC Fifth Assessment Report (AR5), Climate Change 2013: The Physical Science Basis*. Intergovernmental Panel on Climate Change, Geneva, Switzerland.

Kalnay, E., et al., 1996: The NCEP/NCAR 40-year reanalysis project. *Bull. Amer. Meteor. Soc.*, **77 (3)**, 437–471, doi:10.1175/1520-0477(1996)077¡0437:TNYRP¿2.0.CO;2, URL http://dx.doi.org/10.1175/1520-0477(1996)077<0437:TNYRP>2.0.CO;2.

Kiktev, D., J. Caesar, L. V. Alexander, H. Shiogama, and M. Collier, 2007: Comparison of observed and multimodeled trends in annual extremes of temperature and precipitation. *Geophysical Research Letters*, **34 (10)**, n/a–n/a, doi:10.1029/2007GL029539, URL http://dx.doi.org/10.1029/2007GL029539.

Kirtman, B. P. and J. Shukla, 2002: Interactive coupled ensemble: A new coupling strategy for CGCMs. *Geophysical Research Letters*, **29 (10)**, 5–1–5–4, doi:10.1029/2002GL014834, URL http://dx.doi.org/10.1029/2002GL014834.

Mantua, N. J., S. R. Hare, Y. Zhang, J. M. Wallace, and R. C. Francis, 1997: A Pacific interdecadal climate oscillation with impacts on salmon production. *Bull. Amer. Meteor. Soc.*, **78 (6)**, 1069–1079, doi:10.1175/1520-0477(1997)078¡1069:APICOW¿2.0.CO;2, URL http://dx.doi.org/10.1175/1520-0477(1997)078<1069:APICOW>2.0.CO;2.

Martin, G. M., et al., 2011: The HadGEM2 family of Met Office Unified Model climate configurations. *Geoscientific Model Development*, **4 (3)**, 723–757, doi:10.5194/gmd-4-723-2011, URL http://www.geosci-model-dev.net/4/723/2011/.

Mauget, S. A., 2003: Intra- to multidecadal climate variability over the continental United States: 1932–99. *J. Climate*, **16 (13)**, 2215–2231, doi:10.1175/2751.1, URL http://dx.doi.org/10.1175/2751.1.

Maurer, E. P. and H. G. Hidalgo, 2008: Utility of daily vs. monthly large-scale climate data: an intercomparison of two statistical downscaling methods. *Hydrology and Earth System Sciences*, **12 (2)**, 551–563, doi:10.5194/hess-12-551-2008, URL http://www.hydrol-earth-syst-sci.net/12/551/2008/.

Mensing, S., et al., 2013: A network for observing Great Basin climate change. *Eos, Transactions American Geophysical Union*, **94 (11)**, 105–106, doi:10.1002/2013EO110001, URL http://dx.doi.org/10.1002/2013EO110001.

Mignot, J. and S. Bony, 2013: Presentation and analysis of the IPSL and CNRM climate models used in CMIP5. *Climate Dynamics*, **40 (9-10)**, doi:10.1007/s00382-013-1720-1, URL http://dx.doi.org/10.1007/s00382-013-1720-1.

Namias, J., X. Yuan, and D. R. Cayan, 1988: Persistence of North Pacific sea surface temperature and atmospheric flow patterns. *J. Climate*, **1 (7)**, 682–703, doi:10.1175/1520-0442(1988)001¡0682:PONPSS¿2.0.CO;2, URL http://dx.doi.org/10.1175/1520-0442(1988)001<0682:PONPSS>2.0.CO;2.

Peng, S. and J. S. Whitaker, 1999: Mechanisms determining the atmospheric response to midlatitude SST anomalies. *J. Climate*, **12 (5)**, 1393–1408, doi:10.1175/1520-0442(1999)012¡1393:MDTART¿2.0.CO;2, URL http://dx.doi.org/10.1175/1520-0442(1999)012<1393:MDTART>2.0.CO;2.

Rayner, N. A., D. E. Parker, E. B. Horton, C. K. Folland, L. V. Alexander, D. P. Rowell, E. C. Kent, and A. Kaplan, 2003: Global analyses of sea surface temperature, sea ice, and night marine air temperature since the late nineteenth century. *Journal of Geophysical Research: Atmospheres*, **108 (D14)**, n/a–n/a, doi:10.1029/2002JD002670, URL http://dx.doi.org/10.1029/2002JD002670.

Richardson, C. W., 1981: Stochastic simulation of daily precipitation, temperature, and solar radiation. *Water Resources Research*, **17 (1)**, 182–190, doi:10.1029/WR017i001p00182, URL http://dx.doi.org/10.1029/WR017i001p00182.

Roldàn, J. and D. A. Woolhiser, 1982: Stochastic daily precipitation models: 1. a comparison of occurrence processes. *Water Resources Research*, **18 (5)**, 1451–1459.

Ropelewski, C. F. and M. S. Halpert, 1986: North American precipitation and temperature patterns associated with the El Niño/Southern Oscillation (ENSO). *Mon. Wea. Rev.*, **114 (12)**, 2352–2362, doi:10.1175/1520-0493(1986)114¡2352:NAPATP¿2.0.CO;2, URL http://dx.doi.org/10.1175/1520-0493(1986)114<2352:NAPATP>2.0.CO;2.

Schmidt, G. A., et al., 2014: Configuration and assessment of the GISS ModelE2 contributions to the CMIP5 archive. *Journal of Advances in Modeling Earth Systems*, n/a–n/a, doi:10.1002/2013MS000265, URL http://dx.doi.org/10.1002/2013MS000265.

Schneider, U., A. Becker, P. Finger, A. Meyer-Christoffer, B. Rudolf, and M. Ziese, 2011: GPCC full data reanalysis version 6.0 at 1.0°: Monthly land-surface precipitation from rain-gauges built on GTS-based and historic data. URL http://gpcc.dwd.de/, doi:10.5676/DWD$_G PCC/FD_{MV}$6$_1$00.

Stern, R. D. and R. Coe, 1984: A model fitting analysis of daily rainfall data. *Journal of the Royal Statistical Society. Series A (General)*, **147 (1)**, 1–34, URL http://www.jstor.org/stable/2981736.

Taylor, K. E., R. J. Stouffer, and G. A. Meehl, 2011: An overview of CMIP5 and the experiment design. *Bull. Amer. Meteor. Soc.*, **93 (4)**, 485–498, doi:10.1175/BAMS-D-11-00094.1, URL http://dx.doi.org/10.1175/BAMS-D-11-00094.1.

Thompson, D. W. J. and J. M. Wallace, 2000: Annular modes in the extratropical circulation. part I: Month-to-month variability*. *J. Climate*, **13 (5)**, 1000–1016, doi:10.1175/1520-0442(2000)013¡1000:AMITEC¿2.0.CO;2, URL http://dx.doi.org/10.1175/1520-0442(2000)013<1000:AMITEC>2.0.CO;2.

Volodin, E., N. Dianskii, and A. Gusev, 2010: Simulating present-day climate with the INMCM4.0 coupled model of the atmospheric and oceanic general circulations. *Izvestiya, Atmospheric and Oceanic Physics*, **46 (4)**, 414–431, doi:10.1134/S000143381004002X, URL http://dx.doi.org/10.1134/S000143381004002X.

Wang, S.-Y., R. Gillies, L. Hipps, and J. Jin, 2011: A transition-phase teleconnection of the Pacific quasi-decadal oscillation. *Climate Dynamics*, **36 (3-4)**, 681–693, doi:10.1007/s00382-009-0722-5, URL http://dx.doi.org/10.1007/s00382-009-0722-5.

Wang, S.-Y., R. R. Gillies, J. Jin, and L. E. Hipps, 2010: Coherence between the Great Salt Lake level and the Pacific quasi-decadal oscillation. *J. Climate*, **23 (8)**, 2161–2177, doi:10.1175/2009JCLI2979.1, URL http://dx.doi.org/10.1175/2009JCLI2979.1.

Wang, S.-Y., R. R. Gillies, and T. Reichler, 2012: Multidecadal drought cycles in the Great Basin recorded by the Great Salt Lake: Modulation from a transition-phase teleconnection. *J. Climate*, **25 (5)**, 1711–1721, doi:10.1175/2011JCLI4225.1, URL http://dx.doi.org/10.1175/2011JCLI4225.1.

Watanabe, M., et al., 2010: Improved climate simulation by MIROC5: Mean states, variability, and climate sensitivity. *J. Climate*, **23 (23)**, 6312–6335, doi:10.1175/2010JCLI3679.1, URL http://dx.doi.org/10.1175/2010JCLI3679.1.

Wilks, D., 1998: Multisite generalization of a daily stochastic precipitation generation model. *Journal of Hydrology*, **210 (1–4)**, 178 – 191, doi:http://dx.doi.org/10.1016/S0022-1694(98)00186-3, URL http://www.sciencedirect.com/science/article/pii/S0022169498001863.

Wilks, D., 1999a: Interannual variability and extreme-value characteristics of several stochastic daily precipitation models. *Agricultural and Forest Meteorology*, **93 (3)**, 153–169, URL http://www.sciencedirect.com/science/article/pii/S0168192398001257.

Wilks, D., 1999b: Simultaneous stochastic simulation of daily precipitation, temperature and solar radiation at multiple sites in complex terrain. *Agricultural and Forest Meteorology*, **96 (1–3)**, 85 – 101, doi:http://dx.doi.org/10.1016/S0168-1923(99)00037-4, URL http://www.sciencedirect.com/science/article/pii/S0168192399000374.

Wilks, D. S., 2009: A gridded multisite weather generator and synchronization to observed weather data. *Water Resources Research*, **45 (10)**, n/a–n/a, doi:10.1029/2009WR007902, URL http://dx.doi.org/10.1029/2009WR007902.

Wise, E. K., 2010: Spatiotemporal variability of the precipitation dipole transition zone in the western United States. *Geophysical Research Letters*, **37 (7)**, n/a–n/a, doi:10.1029/2009GL042193, URL http://dx.doi.org/10.1029/2009GL042193.

Woolhiser, D. A., 2008: Combined effects of the Southern Oscillation Index and the Pacific Decadal Oscillation on a stochastic daily precipitation model*. *J. Climate*, **21 (5)**, 1139–1152, doi:10.1175/2007JCLI1862.1, URL http://dx.doi.org/10.1175/2007JCLI1862.1.

Xin, X.-G., T.-W. Wu, and J. Zhang, 2013: Introduction of CMIP5 experiments carried out with the climate system models of Beijing Climate Center. *Advances in Climate Change Research*, **4 (1)**, 41–49, doi:10.3724/SP.J.1248.2013.041.

Yukimoto, S., et al., 2012: A new global climate model of the Meteorological Research Institute: MRI-CGCM3 – model description and basic performance. *Journal of the Meteorological Society of Japan*, **90A**, 23–64, doi:10.2151/jmsj.2012-A02.